




## Photon superfluidity through dissipation

G. Keijsers <sup>1</sup>, T. Ham,<sup>1</sup> Z. Geng,<sup>1</sup> K. J. H. Peters <sup>1</sup>, M. Wouters,<sup>2</sup> and S. R. K. Rodriguez <sup>1,\*</sup>

<sup>1</sup>Center for Nanophotonics, *AMOLF*, Science Park 104, 1098 XG Amsterdam, The Netherlands

<sup>2</sup>TQC, *Universiteit Antwerpen*, Universiteitsplein 1, B-2610 Antwerpen, Belgium



(Received 30 June 2023; accepted 2 May 2024; published 10 June 2024)

Superfluidity—frictionless flow—has been observed in various physical systems such as liquid helium, cold atoms, and exciton polaritons. Superfluidity is usually realized by cooling and suppressing all dissipation. Here we challenge this paradigm by demonstrating signatures of superfluidity, enabled by dissipation, in the flow of light within a room-temperature oil-filled cavity. Dissipation in the oil mediates effective photon-photon interactions which are noninstantaneous and nonlocal. Such interactions were expected to severely limit the emergence of superfluidity in conservative photonic systems. Surprisingly, when launching a photon fluid with sufficiently high density and low velocity against an obstacle in our driven-dissipative cavity, we observe a record suppression of backscattering. Our experiments also reveal the reorganization dynamics of photons into a nonscattering steady state and a qualitatively changing behavior of the optical phase as light propagates around the obstacle. The phase is locked between the laser and the obstacle but evolves with the intensity in the wake of the obstacle where the density of the photon fluid and its mean-field interaction energy decrease. Using a generalized Gross–Pitaevskii equation for photons coupled to a thermal field, we model our experiments and elucidate how the noninstantaneous and nonlocal character of interactions influences the suppression of scattering associated with superfluidity. Beyond providing the first signatures of cavity photon superfluidity, and of any superfluid both at room temperature and in steady state, our results pave the way for probing photon hydrodynamics in arbitrary potential landscapes using structured mirrors.

DOI: [10.1103/PhysRevResearch.6.023266](https://doi.org/10.1103/PhysRevResearch.6.023266)

### I. INTRODUCTION

When light encounters an obstacle (a change in impedance), it scatters. This basic feature of optical systems was called into question when Chiao and others predicted that photons in a nonlinear cavity can behave like a superfluid which cannot scatter [1,2]. Interestingly, the temperature of the system seemed to be irrelevant for photon superfluidity to emerge. This contrasts with helium [3,4] and atomic [5–7] systems, where cooling below 2.2 K and  $\approx \mu\text{K}$ , respectively, was needed to reach superfluidity.

Superfluidity requires particle-particle interactions [8]. Since photon-photon interactions are too weak in most systems, photon superfluidity has eluded observation. Circumventing this problem, Carusotto and Ciuti proposed to use exciton-polaritons, hybrid exciton-photon quasiparticles interacting via their exciton part to realize superfluidity in an optical system [9]. Their proposal inspired numerous experiments evincing signatures of polariton superfluidity [10]. However, to date, steady-state room-temperature polariton superfluidity has not been realized. Either cryogenic cooling

[11–19], or excitation with amplified ultrashort laser pulses [20,21], has been required to avoid material bleaching before reaching polariton superfluidity.

Despite numerous claims, the existence of polariton superfluidity under coherent driving is still contested [22]. There are two main reasons for this. First, in all experiments reported to date, backscattering was reduced but not fully suppressed. In particular, in the first and most cited claim of polariton superfluidity, the ratio of scattered-to-transmitted polaritons at an obstacle was only reduced by a factor of three [11]. This contrasts with the zero backscattering expected for superfluidity. Second, in coherently driven systems the phase of the system is fixed by the driving laser. This precludes the spontaneous U(1) symmetry breaking associated with superfluidity. Phase locking to a constant value only occurs in systems homogeneously driven by a single plane wave. For inhomogeneously driven systems, spatial variations in the phase can arise. Indeed, experiments with inhomogeneously and coherently driven polaritons have already shown the nucleation of vortices in regions away from the driving laser, where the phase can evolve [15,23].

Here we present signatures of cavity photon superfluidity. We coherently and inhomogeneously drive an oil-filled cavity and observe a record suppression of backscattering when launching a photon fluid against an obstacle. While we do not observe any backscattering above a critical photon density, based on our measurement dynamic range we estimate a backward-to-forward scattering ratio suppression of at least 900-fold compared with the linear regime. In addition,

\*s.rodriguez@amolf.nl

through interferometric measurements we show qualitative differences in the evolution of the optical phase in front of and behind the obstacle. The phase is locked between the laser and the obstacle, but it evolves in the wake of the obstacle as the intensity increases due to the suppression of backscattering.

The physics of our system is qualitatively different from that of conventional polariton systems. In our oil-filled cavity, particle-particle interactions are mediated by heat dissipation. Thus, paradoxically, we observe the first signatures of cavity photon superfluidity by heating rather than cooling the system. Furthermore, effective interactions in thermo-optical systems, like ours, are noninstantaneous and nonlocal because of thermal relaxation and diffusion [24–26]. Neglecting driving and dissipation, similar interactions were predicted to severely reduce the critical velocity for photon superfluidity [27] and thereby preclude its observation. However, for a driven-dissipative thermo-optical cavity, the prospect of superfluidity has not been addressed. This prospect poses a conceptual challenge since superfluidity is generally associated with the absence of dissipation. However, the interactions needed for superfluidity in a thermo-optical cavity are due to absorption and the resultant heat dissipation.

Superfluid-like behavior induced through dissipation has been demonstrated in systems where the propagation of light along a spatial coordinate is mapped to the time evolution of a photon fluid [28–39]. Those systems are generally described by a conservative Gross–Pitaevskii type equation for an equilibrium fluid. Time is replaced by the propagating spatial coordinate, and dissipation does not enter the equation despite being directly responsible for the effective photon-photon interactions. Consequently, the emergence of superfluid-like behavior in those systems is independent of their dissipative dynamics. In contrast, cavity experiments involve photon or polariton fluids propagating in space and time. The properties of such optical fluids are fully determined by the balance between driving and dissipation. Crucially, in the presence of a thermo-optical nonlinearity as explored in this work, light absorption and heat dissipation result not only in particle loss. Thermal dynamics induce noninstantaneous effective photon-photon interactions which, as we show, make the physics of superfluidity different than in the propagating beam configuration.

## II. EXPERIMENTAL SETUP

Figure 1(a) illustrates our setup: a Fabry–Pérot cavity filled with cinnamon oil. The oil partly absorbs the intracavity light. This generates heat, which decreases the oil’s density and refractive index. The resultant intensity-dependent refractive index, a thermo-optical nonlinearity, effectively mediates repulsive photon-photon interactions. The cavity is made by two distributed Bragg reflectors (DBRs) with 99.9% reflectance at 532 nm, our laser wavelength. One of the mirrors is fixed. We control the position and orientation of the other mirror using a six degree of freedom piezoelectric actuator. This enables us to align the mirrors parallel to each other and to precisely control their separation.

For the measurements aimed at revealing the scattering of a photon fluid off an obstacle, we illuminate the cavity resonantly or quasiresonantly using a 532 nm single-mode

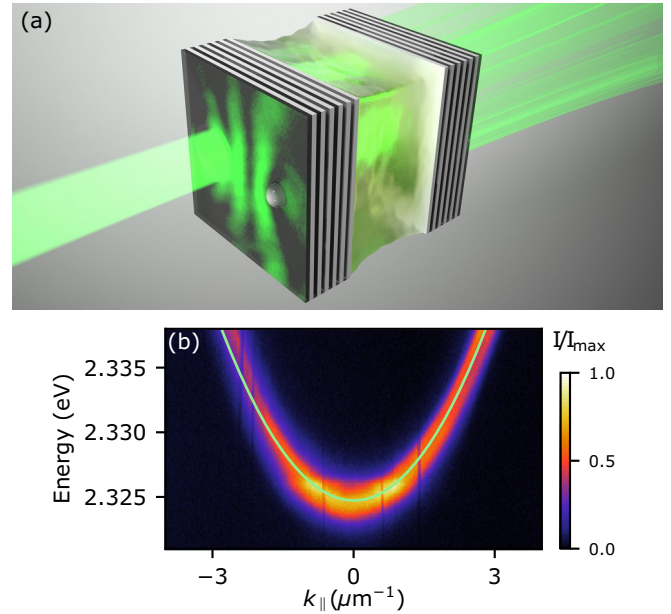


FIG. 1. (a) An oil-filled cavity formed by two dielectric mirrors is driven by a continuous-wave laser. The gray bump on the left mirror represents an obstacle. Light scattering off this obstacle interferes with the incident flow and forms fringes. (b) Dispersion relation for intracavity photons obtained from white light transmission measurements. The solid line is a parabolic fit.

continuous-wave laser. We control the laser amplitude using an electro-optic modulator. About 4% of the modulated light is directed to a photodetector for monitoring purposes. The rest of the light is injected to and then collected from the cavity using 20 $\times$  microscope objectives with a numerical aperture (NA) of 0.4. The beam diameter half fills the back aperture of the objective. Hence, the distribution of light angles and momenta sent into the cavity has a width given by roughly half of the NA. We analyze the cavity transmission in position and momentum space simultaneously using a single high-speed camera (Phantom VEO E-310L), as illustrated in Appendix A. We used one instead of two cameras for position- and momentum-space measurements to avoid synchronization issues, which are more likely to occur at the high speed of our measurements.

The obstacle used to probe the scattering properties of the photon fluid was created in one of our mirrors via laser writing [40]. That mirror contains an additional 30 nm silicon layer between the glass substrate and the DBR. We created the obstacle by illuminating the silicon layer with our laser from the substrate side. The incident power was 50 mW, tightly focused with the microscope objective. The absorbed laser power causes the silicon to expand, which in turn permanently deforms the adjacent DBR. The induced deformation locally changes the cavity length and creates a repulsive obstacle, i.e., a hill in the potential-energy landscape for photons. The lateral dimensions of the obstacle probed in the experiments are 2 and 4  $\mu\text{m}$  along and perpendicular to the flow direction, respectively. The obstacle is roughly 50 nm high, but the exact height is irrelevant to our results as long as the photon

fluid cannot go over the obstacle, which is the case in our experiment.

Beyond providing a means to tailor the potential landscape for photons, the silicon layer does not play a role in our experiments. The power per unit area required to deform it and the adjacent DBR is well above that needed to observe all nonlinear effects reported in this paper. Indeed, in the absence of oil, none of the nonlinear effects reported ahead arise. Furthermore, in Appendix B we show that our measurements are reproducible across the transition to the nonlinear regime where scattering is suppressed. This means that the suppression of scattering does not involve irreversible changes to the potential landscape. In contrast, the deformation of the silicon layer and the adjacent DBR is an irreversible process.

For the measurements aimed at probing the phase evolution of the photon fluid, the cavity transmission is made to interfere with a uniform reference beam. The reference beam is created by placing a beam splitter at the output of the laser. That beam is then expanded and directed to the camera. The main beam was modulated at 20 kHz into a square wave with  $P_{\max} = 180$  mW, by a modulator after the beam splitter. The reference beam was chopped at 2 kHz with a 50% duty cycle. The chopping allowed us to alternate between recording a series of images of only the cavity transmission and recording its interference with the reference beam. This was necessary because, at the high frame rate at which we operated the camera (500 kHz), the number of usable pixels is strongly reduced. Hence, to not further compromise spatial resolution, we alternated between different types of image in time. The relatively high chopping frequency was chosen to avoid the effects of noise, which are important below  $\approx 100$  Hz.

Our setup also enables us to measure the dispersion relation of photons in the cavity. To this end, the cavity is illuminated with white light, and the transmission is directed to a spectrograph. To analyze the momentum of the transmitted light, we imaged the back focal plane of the collection objective on the slit of the spectrograph. In this way, a crosscut in the two-dimensional momentum space is selected from the cavity transmission, which is subsequently dispersed in energy by a grating. The resulting energy-momentum relation is imaged on the spectrograph camera. The measured cavity photon dispersion is shown in Fig. 1(b). The observed parabolic dispersion corresponds to free photons with an effective mass  $m^*$  on the order of  $10^{-35}$  kg. The ground-state energy depends on the cavity length, which we can tune using piezoelectric actuators displacing one of the cavity mirrors.

### III. RESULTS

#### A. Density-dependent photon scattering

The emergence of superfluidity is characterized by the suppression of scattering above a critical density and below a critical velocity. To test this in our system, we launched photon fluids with different densities and velocities toward the obstacle and measured the transmitted intensity in position and momentum space. The density and direction of the injected photons are determined by the incident laser power and angle, respectively.

Figures 2(a)–2(h) show the density-dependent scattering off the obstacle. These experiments were done with a constant cavity length such that the laser frequency is blue-detuned from the ground state. The laser amplitude was modulated sinusoidally at 150 Hz. Figure 2(a) shows optical hysteresis and bistability of the total transmitted intensity, when scanning the laser power up and down; this evinces effective photon-photon interactions in our system.

Figures 2(b) and 2(c) show the spatially dependent transmission at two points of the hysteresis cycle, indicated by the colored symbols in Fig. 2(a). Incident powers are similar in Figs. 2(b) and 2(c), but spatial patterns differ substantially. At low density, Fig. 2(b) shows fringes due to interference between the incident flow and scattering off the obstacle. Figure 2(c) shows that these fringes disappear at high density, indicating that scattering from the obstacle has been reduced. Figure 2(d) shows cuts of Figs. 2(b) and 2(c) along the flow axis, evincing the intensity-induced suppression of interference fringes more clearly.

As backscattering from the obstacle is reduced at high intensity, light begins to flow around the obstacle. One can recognize this, for example, by noticing the greater intensity in the top-right quadrant of Fig. 2(c) relative to Fig. 2(b). Because of cavity losses, the photon fluid does not reach the wake of the obstacle. The distance from the laser spot to the wake of the obstacle is greater than the propagation length, which is limited by the aforementioned losses. Nonetheless, for a reduced laser-obstacle distance as considered in Sec. III F, light can indeed reach behind the obstacle.

Figures 2(e)–2(h) show momentum-space measurements for the same driving conditions as in Figs. 2(a)–2(d). In Fig. 2(e) we plot the ratio of backward scattering off the obstacle to forward flow,  $I_B/I_F$ , versus the incident power. Appendix C explains the procedure for calculating  $I_B/I_F$  from momentum-space measurements. Figure 2(e) shows that backscattering is reduced when crossing the bistability in the forward scan, and remains low throughout the entire high-density branch. A qualitatively similar suppression of backscattering occurs for polaritons in the high-density bistable state [9,10,41]. Figures 2(f) and 2(g) show momentum distributions for two cases, corresponding to Figs. 2(b) and 2(c). Figure 2(h) shows cuts along  $k_y = 0$ . Overall, these measurements demonstrate how the Rayleigh scattering ring collapses and the backscattering peak (see orange and purple arrows) diminishes at high density. A stronger suppression of backscattering is shown in Sec. III C.

To gain further insight into the physics, we developed a model of our system comprising a driven-dissipative Gross–Pitaevskii equation for photons coupled to a thermal field (see Appendix D). We first validated our model by (qualitatively) reproducing our experimental observations. Numerical results in Figs. 2(i)–2(p) demonstrate the bistability, Rayleigh ring collapse, and backscattering reduction at high density, as observed in Figs. 2(a)–2(h).

While our simulations qualitatively reproduce our experimental observations, quantitative differences remain. First, experiments show a larger suppression of backscattering than simulations. We are unsure about the origin of this effect. We believe that additional slow nonlinearities in the oil, not accounted for in our model, may be playing a role. Our belief

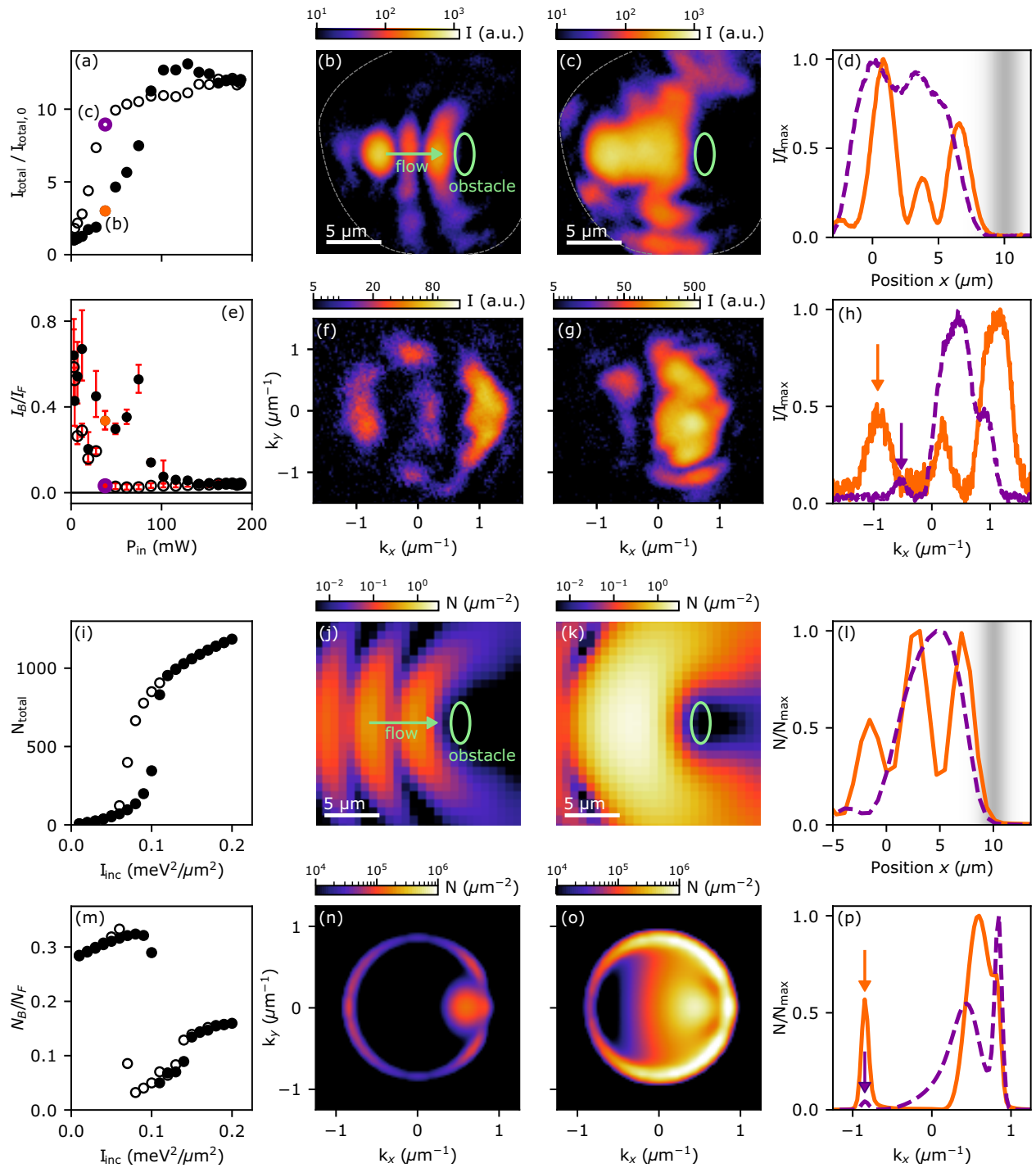


FIG. 2. Panels (a)–(h) are experimental measurements, and panels (i)–(p) are numerical simulations using the model described in Appendix D. (a) Solid and open circles are the total transmitted intensity  $I_{\text{total}}$  when ramping the incident laser power  $P_{\text{in}}$  up and down, respectively.  $I_{\text{total}}$  is divided by its value at the lowest laser power,  $I_{\text{total},0}$ . (b), (c) Spatially dependent transmitted intensity at the states indicated in panel (a). (d) Solid and dashed curves are the intensity  $I$  along the flow axis passing through the center of the laser spot and of the obstacle in panels (b) and (c), respectively, divided by its maximum value  $I_{\text{max}}$ . (e) Backward-to-forward intensity scattering ratio (see Appendix C for details),  $I_B/I_F$ , when ramping the laser power up and down. Panels (f) and (g) are momentum-space images of the transmitted intensity corresponding to panels (b) and (c), respectively. (h) Cuts along  $k_y = 0$  in panels (f) and (g). Arrows in panel (h) indicate backscattered momenta. (i)–(p) Same as panels (a)–(h) but for the calculations. In (i) we plot the total number  $N_{\text{total}}$  of photons in the simulation area. In panels (j), (k), (n), and (o) we plot the photon density  $N = |\psi|^2$ . In panel (m) we plot the backward-to-forward photon-scattering ratio  $N_B/N_F$ . In panels (l) and (p) we plot the photon density along the flow axis and  $k_y = 0$ , respectively, both referenced to the maximum value. Green circles in panels (b), (c), (j), and (k), and shaded areas in panels (d) and (l) indicate the obstacle location and size. The thin dashed gray curves in panels (b) and (c) indicate the edge of a pinhole in the collection path. The pinhole was needed to avoid overlap between position- and momentum-space measurements, which were recorded simultaneously using the same camera.

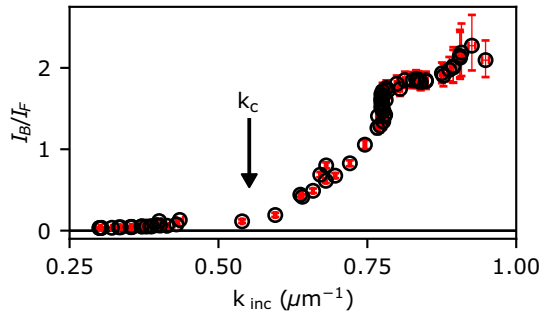


FIG. 3. Backward-to-forward scattering ratio when slowly increasing the fluid's mean incident momentum.  $k_c$  is the critical momentum.

is based on the observation (reported in Appendix B) that the intensity in the wake of the obstacle slightly decreases over long timescales; such an effect is absent in our model and points to the likely presence of additional slow nonlinearities. Second, the experimental data exhibit a shift in the backscattering wave vector that is not present in the simulations [see arrows in Figs. 2(h) and 2(p)]. We believe that two features of the experiment are responsible for this discrepancy. On one hand, the momentum distribution in the linear regime has a peak near  $k_x = 0$  which is not present in the simulations. That peak likely originates from disorder in the sample, which is not included in the model. On the other hand, the suppression of scattering predicted by the model is greater than what we can experimentally detect given our limited signal-to-noise ratio. Thus, the (shifted) backscattered wave vectors we observe experimentally could be due to that disordered-induced scattering, and not to the backscattering of the incident flow. While all these effects and the additional nonlinearities discussed above warrant further study, the qualitative agreement between experiments and simulations nonetheless encourages the use of our model for elucidating the mechanisms underlying the intensity-induced scattering suppression. In that spirit, we also verified via numerical simulations that our results are indeed insensitive to the height of a repulsive obstacle.

### B. Observation of a critical velocity for superfluidity

Figure 3 shows  $I_B/I_F$  versus the mean incident momentum  $k_{inc}$  at constant power, evincing the existence of a critical momentum below which backscattering is suppressed. For these measurements, we fixed the laser power to  $P_{in} = 72$  mW and slowly increased the cavity length. The change in cavity length shifts in energy the parabolic dispersion relation for photons. Consequently, since the incident light has constant frequency and broad momentum distribution, different wave vectors are injected as the cavity length changes. Appendix E explains how  $I_B/I_F$  and  $k_{inc}$  were extracted from momentum-space measurements. Since the in-plane momentum  $k_{||}$  determines the cavity photon velocity  $v = \hbar k_{||}/m^*$ , Fig. 3 demonstrates the existence of a critical velocity, as expected for superfluidity [42].

The mechanisms determining the critical velocity of our driven-dissipative system are different from those of conservative superfluids [5–7,27,32,42–44]. In particular, unlike in conservative systems, in our system the suppression of

scattering is strongly influenced by driving, dissipation, and heat diffusion corresponding to effective nonlocal interactions. Comparisons of our system to other driven-dissipative systems, like cavity polaritons, could be interesting. However, measurements like those in Fig. 3 have never been reported for polariton systems. Signatures of a critical velocity have indeed been observed in polariton systems. Typically, these are found in the form of two measurements, one above and one below the critical value [11,20,21]. However, a quantification of the scattering as a function of  $k_{inc}$ , necessary for the identification of a well-defined threshold for backscattering suppression, has never been experimentally reported.

### C. Record suppression of backscattering

The results presented in Figs. 2(a)–2(h) demonstrate how scattering off an obstacle is reduced at high photon density. Since the reduction of scattering was evinced in the suppression of interference fringes between the laser spot and the obstacle, a large laser-obstacle separation combined with a relatively large flow velocity was necessary to observe multiple fringes and their suppression. However, the large laser-obstacle separation combined with the losses of our system prevents much of the intensity to reach the obstacle. These conditions, combined with the high flow velocity, prevented the backscattering from being further suppressed.

In an effort to fully suppress the backscattering, we performed similar measurements as in Figs. 2(a)–2(h) but at a smaller laser-obstacle distance and at a reduced velocity. These conditions enable more intensity to reach the obstacle, albeit the number of fringes at low density in real space is reduced. The disappearance of fringes in real-space images, indicating the suppression of backscattering, is therefore visually less striking for these measurements than in Figs. 2(b)–2(d). However, as we show next, the suppression of backscattering at high density is significantly enhanced by the reduced velocity and closer proximity of the laser spot to the obstacle. The results are shown in Fig. 4, with all intensities plotted in a logarithmic scale.

Figures 4(a) and 4(b) show position- and momentum-space measurements, respectively, along the flow axis. Measurements in the full two-dimensional position and momentum space, from which the cuts in Figs. 4(a) and 4(b) are extracted, are presented in Appendix F. Solid and dashed curves in Figs. 4(a) and 4(b) correspond to low- and high-density states, respectively. The number of interference fringes at low density is smaller in Fig. 4(a) than in Fig. 2(d) because of the reduced photon momentum and the shorter laser-obstacle distance. These driving conditions enable a stronger suppression of scattering at high density. Indeed, the dashed curve in Fig. 4(a) shows complete absence of scattering-induced interference fringes across the dynamic range of our measurement, which spans almost three orders of magnitude.

Figure 4(b) shows momentum-space measurements corresponding to Fig. 4(a). At high photon density, the center of the forward momentum peak shifts to a lower momentum. The shift is due to the interaction-induced blueshift, which at fixed frequency results in lower kinetic energy. The most interesting effect, however, is the suppression of the backscattering peak at high density. We are unsure if the backscattering

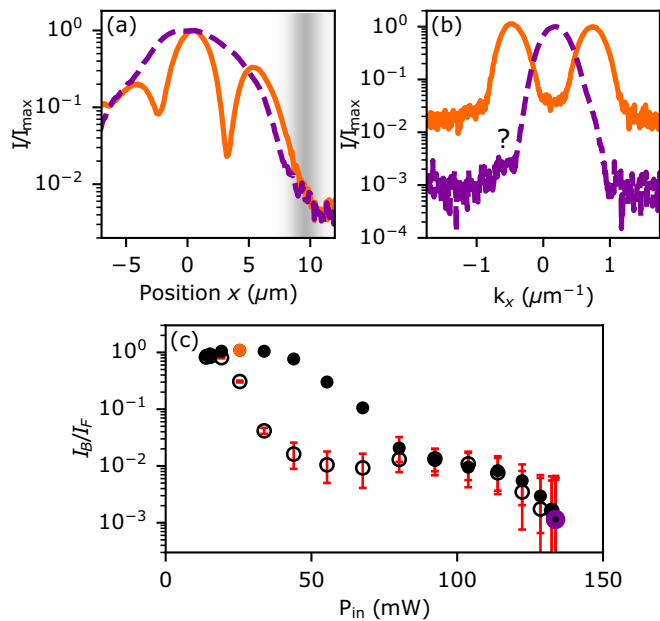


FIG. 4. (a) Solid and dashed curves are measurements of the photon density along the flow axis at low and high density, respectively. The flow velocity is lower than in Figs. 2(a)–2(h). (b) Momentum-space measurements corresponding to panel (a), evincing a full suppression of the backscattering peak initially at  $k_x \approx -0.5 \mu\text{m}^{-1}$ . (c) Solid and open circles are the backward-to-forward scattering ratio when ramping the laser power up and down, respectively. Orange and purple solid circles correspond to the two cases in panels (a) and (b).

suppression is complete. The momentum-space measurements possibly display a tiny shoulder on the tail of the distribution of the forward flow, under the question mark in Fig. 4(b). We are unsure if this tiny feature corresponds to backscattering or to just noise. Assuming the former, we claim a lower bound on the suppression of backscattering. We estimate this lower bound based on the values of  $I_B/I_F$  as a function of the incident power, shown in Fig. 4(c). Since  $I_B/I_F \approx 1.09$  in the linear regime, and  $I_B/I_F \approx 0.0012$  in the nonlinear regime, the reduction in  $I_B/I_F$  is at least a factor of 900. This backscattering reduction is at least two orders of magnitude greater than what was reported in the first claim of polariton superfluidity at cryogenic temperatures in 2009 [11], and at room temperature (without steady state) in 2017 [20].

Interestingly, the laser power needed to achieve this effect is only 40 mW. This power is comparable to, and in many cases even smaller than, input powers needed for polariton superfluidity [15,16,45]. This is remarkable considering that our cavity quality factor is roughly one order of magnitude smaller than in typical polariton experiments. In Appendix G we present a calculation of the temperature rise  $\Delta T$  in the oil at 40 mW, in the upper branch of the bistability; we find  $\Delta T = 2^\circ\text{C}$ .

#### D. Dynamics of a photon fluid reorganizing into a nonscattering steady state

Interactions in our system are noninstantaneous because of the finite thermal relaxation time of the oil. Essentially, the

photon field is coupled to a slowly varying thermal field and this makes the effective photon-photon interactions noninstantaneous. A similar coupling between fast and slowly varying degrees of freedom has been considered in the context of coherently driven polaritons [16,46,47]. However, unlike in our system, in those systems both instantaneous and noninstantaneous interactions are simultaneously present. The former are due to polariton-polariton interactions, while the latter are due to interactions between polaritons and excitons comprising the so-called exciton reservoir. Because the relaxation time of the exciton reservoir is not nearly as long as the thermal relaxation time in our system, it turns out that the contributions to the blueshift from instantaneous and noninstantaneous interactions are of similar magnitude in polariton systems. In contrast, in our system only noninstantaneous interactions contribute to the blueshift. Thus, our system operates in a regime in which, as far as we know, superfluidity has not been considered.

Figures 5(a)–5(d) and 5(e)–5(h) show measurements and simulations, respectively, of light propagating toward the obstacle when the laser power changes abruptly from well below to well above the bistability. For the experiments, we modulated the laser amplitude into a square wave with maximum power  $P_{\text{max}} = 130$  mW, and used a camera acquisition rate of 500 kHz. The laser power rises within 3  $\mu\text{s}$ , which is much less than the thermal relaxation time  $\tau_T$ . Such a step-like power increase enables us to characterize the reaction time of the system. Figures 5(b) and 5(a) show the spatially resolved transmitted intensity 6  $\mu\text{s}$  and 120  $\mu\text{s}$ , respectively, after the power step at  $t = 0$ . In Fig. 5(b) the nonlinearity has not fully developed. Consequently, we observe two fringes due to the interference of the incident flow and scattering off the obstacle. Figure 5(a) shows that, at longer times, interference fringes disappear.

To evince the disappearance of interference fringes at long timescales more clearly, in Fig. 5(c) we present cuts of Figs. 5(a) and 5(b) along the flow axis ( $y = 0$ ). The cuts in Fig. 5(c) show the presence of two fringes at short times, and zero fringes at long times when the nonlinearity has fully developed and scattering from the obstacle has been suppressed. Figure 5(d) presents a more detailed characterization of the experimental time-resolved transmitted intensity along the flow axis ( $y = 0$ ). Notice how the photon fluid reorganizes long after the laser power has increased and settles into a steady state with no interference fringes consistent with superfluidity.

Simulations in Figs. 5(e)–5(h) qualitatively reproduce our experimental observations. Time in the simulated data is divided by the thermal relaxation time  $\tau_T$  in our model. With this division we highlight that the results in Fig. 5(h) are independent of the value of  $\tau_T$ , provided  $\gamma^{-1} \ll \tau_T$  with  $\gamma$  the dissipation rate. Overall, Fig. 5 shows that thermal dynamics only matter on timescales commensurate with  $\tau_T$ . Afterwards, a steady state without scattering sets in. The time to reach this steady state in the simulations is  $t/\tau_T \approx 3$ . This is roughly in agreement with experiments, where a steady state is reached around 60  $\mu\text{s}$ , corresponding to roughly three-to-four times the thermal relaxation time of the oil [48].

While experimental and numerical data in Fig. 5 are in qualitative agreement, the length scales over which the

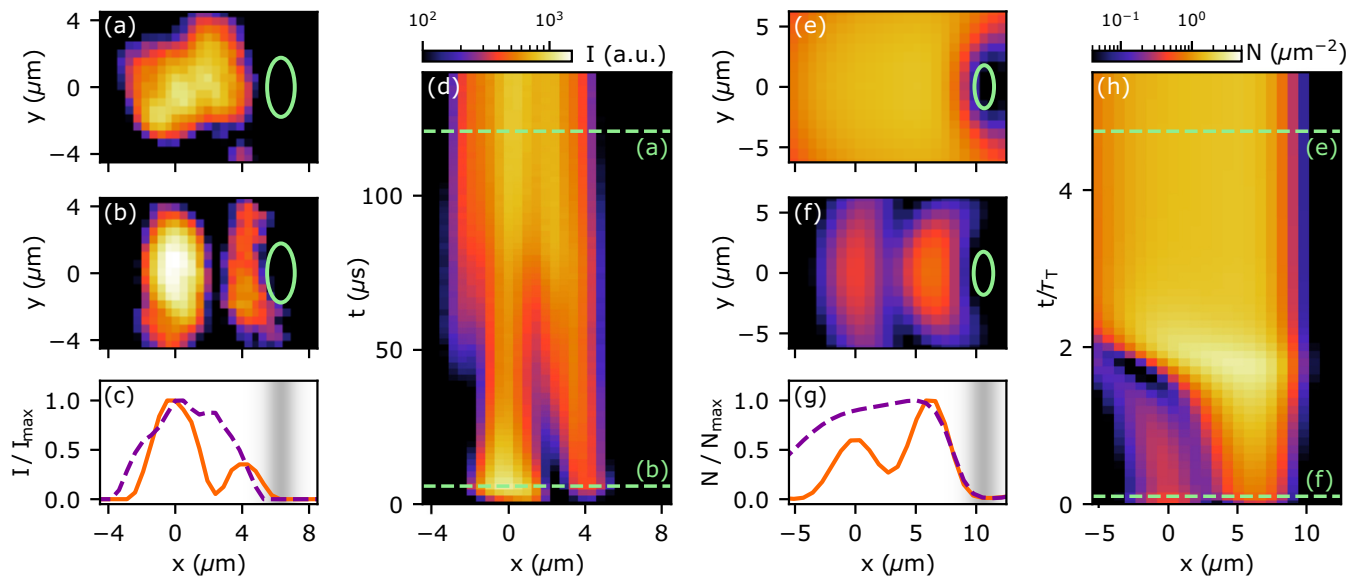


FIG. 5. Panels (a)–(d) are experimental measurements, and panels (e)–(h) are the corresponding numerical simulations. (a), (b) Spatially dependent transmitted intensity at the times indicated by the dashed lines in panel (d). Around  $t = 0$ , the laser power is increased to its maximum value within  $3 \mu\text{s}$ , which is well below the thermal relaxation time. Panel (a) corresponds to the steady state, and panel (b) corresponds to a transient regime shortly after the sudden increase in power. (c) Normalized transmitted intensity along the flow axis ( $y = 0$ ) in panels (a) and (b), indicated by dashed and solid lines, respectively. (d) Transmitted intensity along flow axis ( $y = 0$ ) as a function of time. (e)–(h) Same as in panels (a)–(d) but for the calculated photon density. Both measurements and simulations show the disappearance of interference fringes as a steady state emerges.

observed phenomenology occurs are slightly different (by about 20%). This difference might be due to experimental limitations. In particular, the signal-to-noise ratio and spatial resolution are limited by the high frame rate at which we image our system. Other possible origins of the slightly different length scales are the aforementioned additional slow nonlinearity in the oil, and disorder in the experimental sample. Imperfections in the cavity mirrors (not included in the model) can introduce losses that limit the propagation distance of the photon fluid and result in smaller features in experiments than in simulations.

### E. Nonlocal interactions mediated by heat diffusion suppress light scattering

Interactions in our system are nonlocal because of heat diffusion in the oil. Essentially, the photon field generates a thermal field that can have a different spatial profile because of heat diffusion. This makes the effective photon-photon interactions nonlocal in space [24–26]. Effects of such nonlocal interactions on superfluidity have been studied in conservative photonic systems [27], and in analog systems where the spatial propagation of a light beam through a nonlinear medium is mapped to the time evolution of a fluid [30,31,34–36,39]. In both of those configurations, where coherent driving and dissipation are irrelevant, nonlocal interactions severely reduced the critical velocity for superfluidity. In contrast, we show next that diffusion can actually reduce the scattering of a photon fluid off an obstacle.

We investigate the effects of heat diffusion numerically, since experiments have very limited tunability over the diffusion constant. Figures 6(a) and 6(b) show the spatially

resolved photon density for two values of the diffusion constant  $D_T$ . The corresponding diffusion length is  $l_D = 1 \mu\text{m}$  in Fig. 6(a), and  $l_D = 16 \mu\text{m}$  in Fig. 6(b). The profiles of temperature change  $\Delta T$  corresponding to Figs. 6(a) and 6(b) are shown in Figs. 6(c) and 6(d), respectively. Temperature and photon density profiles are similar for small  $l_D$  but differ for large  $l_D$ . The latter evinces that the dissipation-induced blueshift of the photon energy depends not only on the local intensity, but also on the surrounding intensity—the defining feature of nonlocality.

Figure 6(e) shows the number of intracavity photons versus the incident power, similar to Fig. 2(i). Orange and purple symbols correspond to  $l_D = 1 \mu\text{m}$  and  $l_D = 16 \mu\text{m}$ , respectively. The simulations show that the bistability is wider, and centered at a greater intensity, for larger  $l_D$ . Figure 6(f) shows the corresponding backward-to-forward density,  $N_B/N_F$ , similar to  $I_B/I_F$ . Overall, we observe that stronger diffusion changes the temperature across a larger area. Consequently, more laser power is needed to generate the mean-field interaction energy needed for the suppression of scattering. The bistability is therefore shifted to a larger intensity for larger  $l_D$ , as Fig. 6(e) shows. However, once the high-density state of the bistability is reached, the reduction of backscattering is more substantial for a larger diffusion constant [see Fig. 6(f)].

Our results illustrate how one type of dissipation (light absorption resulting in heat) effectively reduces another type of dissipation (scattering off the obstacle). The absorbed and dissipated light enables the remaining light to flow without scattering. Backscattering suppression is less pronounced in simulations than in experiments. We are unsure about this discrepancy. We tentatively attribute it to limitations of our model, including the possible relevance of unaccounted slow

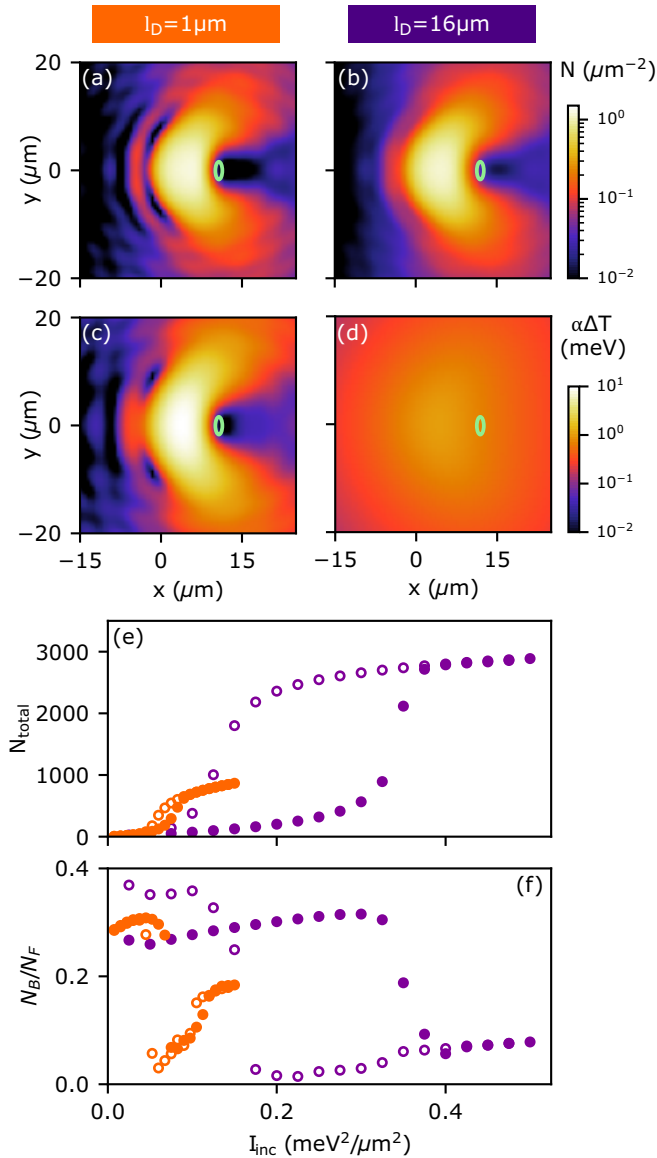


FIG. 6. Calculated photon density for a diffusion length of (a)  $l_D = 1 \mu\text{m}$  and (b)  $l_D = 16 \mu\text{m}$ . Panels (c) and (d) are the temperature change profiles corresponding to panels (a) and (b), respectively. (e), (f) Orange and purple symbols correspond to  $l_D = 1 \mu\text{m}$  and  $l_D = 16 \mu\text{m}$ , respectively. Solid and open circles correspond to an increasing and decreasing, respectively, ramp of the laser power. (e) Total number of intracavity photons versus incident power, and (f) corresponding backward-to-forward scattering ratio evincing that the maximum suppression of backscattering is greater for a larger diffusion length.

nonlinearities in the oil as explained in Sec. III A. Experiments were reproduced multiple times and for different flow conditions.

### F. Intensity-dependent spatial phase variations

In a superfluid, the phase can evolve freely. This enables superfluidity to emerge with a random phase at a  $U(1)$  symmetry-breaking transition, and to break down via the generation of quantized vortices [49]. Despite many similarities between conservative and driven-dissipative su-

perfluids, a crucial difference arises in the evolution of the phase when coherent driving is involved. In coherently and homogeneously driven systems, the phase of the system is fixed everywhere by the driving laser. Phase dislocations can therefore not emerge. Partly for this reason, it has been argued that scattering reduction in coherently and homogeneously driven polaritons should be associated with the emergence of a rigid state rather than a superfluid [22]. Here, it is important to stress that phase locking to a constant value everywhere only occurs in systems driven homogeneously in space and time. When driving inhomogeneously in time with pulses [14,20,23,50], or inhomogeneously in space with a localized laser spot [15,18,23,45,51–53], signatures of free phase evolution, such as vortices, can emerge. In light of these results and considerations, we proceed to investigate how the phase of our coherently but inhomogeneously driven photonic system evolves in time and space across the intensity-induced scattering suppression.

Figure 7 shows measurements for a photon fluid propagating toward the obstacle. The laser power was abruptly increased, as in Fig. 5. Each column corresponds to a time elapsed, indicated on top, since the step-like power increase. The top row shows the spatially dependent transmitted intensity. Middle and bottom rows show mutually identical interferometric measurements, obtained by interfering the cavity transmission with an expanded laser beam providing a uniform reference phase. We present the interferometric measurements twice to include the dashed curves in the bottom row, while providing an unobstructed view of the data in the middle row. The dashed curves indicate fringe maxima. In principle, the spatially dependent phase of the fluid can be extracted from these interferometric measurements. However, since the photon density in the wake of the obstacle is low, the phase value is extremely sensitive to details of the phase-extraction algorithm and it is prone to errors. Moreover, we are not interested in the value of the phase itself. We are simply interested in assessing whether the phase is locked to a constant value everywhere, or spatial variations can arise with changes in intensity.

The first column in Fig. 7 shows that, immediately after the laser power rises, very little density flows beyond the obstacle; notice the dark region along the flow axis and behind the obstacle, enclosed by the dashed semicircle. Meanwhile, to the left of the obstacle, we observe fringes due to interference between the incident flow and scattering off the obstacle. Interferometric measurements below show undisturbed phase fronts, with low fringe contrast where the density is low. At  $6 \mu\text{s}$ , light begins to flow around the obstacle; see, for example, the curved green arrow. Since light has just started to flow beyond the obstacle, fringes in the interferogram have only slightly changed. At  $10 \mu\text{s}$ , the top row shows that a significant density has reached the region behind the obstacle. The contrast of the interference fringes resulting from backscattering has also decreased. Meanwhile, interferometric measurements below show some changes. However, the presence of phase dislocations is still ambiguous due to the low fringe contrast. Finally, by  $54 \mu\text{s}$  the system is settled into a steady state. The top row shows that fringes due to backscattering have vanished, and the steady-state density behind the obstacle is significant. The interferogram shows phase dislocations in the



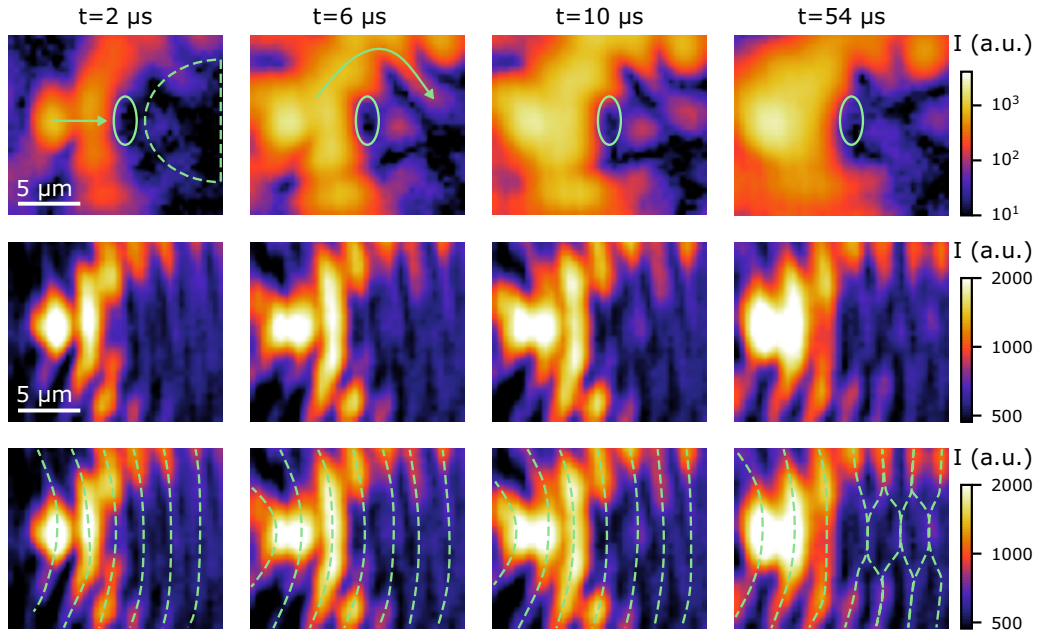


FIG. 7. Cavity transmission real-space images and interferograms. For these experiments, the input power was suddenly increased, as it was done in Figs. 5(a)–5(d). Each column corresponds to a different time (indicated on top) after the power increase. (top row) Spatially dependent transmitted intensity. The ellipse indicates the approximate location of the obstacle. The dashed semicircle roughly encloses the region we refer to as “in the wake of the obstacle.” (middle row) Fringe patterns resulting from the interference between the transmitted intensity and an expanded laser beam providing a uniform reference phase throughout the measurement space. (bottom row) Same data as in the middle row, but with dashed green curves as guides to the eye indicating fringe maxima.

wake of the obstacle, where the density of the photon fluid and its mean-field interaction energy decrease. The dislocations are highlighted by the green dashed curves in the bottom row. In Appendix H we show phase dislocations when light flows onto the obstacle at another angle, thereby demonstrating the generality of this phenomenon.

In Fig. 8 we illustrate how the interferogram features evolve as light propagates around the obstacle. To that end, we analyze the intensity in the real-space images and interferograms of Fig. 7, along the path indicated by the blue lines in Figs. 8(a) and 8(c). The measurements in Figs. 8(a) and 8(c) are exactly the same as those in the top and middle row of the leftmost column in Fig. 7, but now with the path under consideration indicated. We select four times for our analysis: 2, 6, 10, and 14  $\mu$ s after the step-like power increase. Measurements at these four times and along the aforementioned path are presented in Figs. 8(b) and 8(d). The region behind the obstacle is indicated by the shaded area in Figs. 8(b) and 8(d).

Figure 8(b) shows that the intensity behind the obstacle increases by nearly two orders of magnitude between 2 and 14  $\mu$ s. This demonstrates the ability of light to flow around and past the obstacle as scattering is suppressed. Figure 8(d) then shows how the interferogram evolves as the light intensity surrounds the obstacle. Notice the interferogram peak behind the obstacle (shaded region) shifts with time. This shift can only be due to a change in the local phase, thereby demonstrating absence of phase locking in that region.

We now present a more detailed analysis of the data in Fig. 8(d), in order to demonstrate the qualitatively different behavior of the phase in front and behind the obstacle. In

Fig. 8(e) we plot the difference in intensity between two interferograms 4  $\mu$ s apart. We evaluate this difference along the same path indicated by the blue lines in Figs. 8(a) and 8(c). If a local maximum in this intensity difference plot remains unchanged, the phase therein is locked. In contrast, if a local maximum shifts, the phase therein has evolved.

Figure 8(e) shows that, in front of the obstacle, fringe maxima align with the blue rectangles. The phase in that region is locked; it does not evolve with the changing intensity. In contrast, behind the obstacle, the peak in the interferogram gradually shifts over time. For clarity, we indicated the peak location with a vertical line of the same color as each curve. The analysis thus shows that, unlike in homogeneously and coherently driven systems, the phase behind the obstacle is not locked. It evolves with the changing intensity. However, the phase is not entirely free either as in incoherently driven systems such as lasers and polariton condensates. In those systems, the phase is spontaneously selected at the U(1) symmetry-breaking transition where a coherent-state emerges. Our inhomogeneously and coherently driven photon fluid is thus in an interesting intermediate regime that warrants further experimental and theoretical studies.

#### IV. CONCLUSIONS AND PERSPECTIVES

In summary, we demonstrated signatures of photon superfluidity in the behavior of light as it encounters an obstacle. Above a critical intensity and below a critical velocity, backscattering from the obstacle is suppressed. Furthermore, we showed that the optical phase is locked between the laser and the obstacle but evolves with the rise in intensity in the

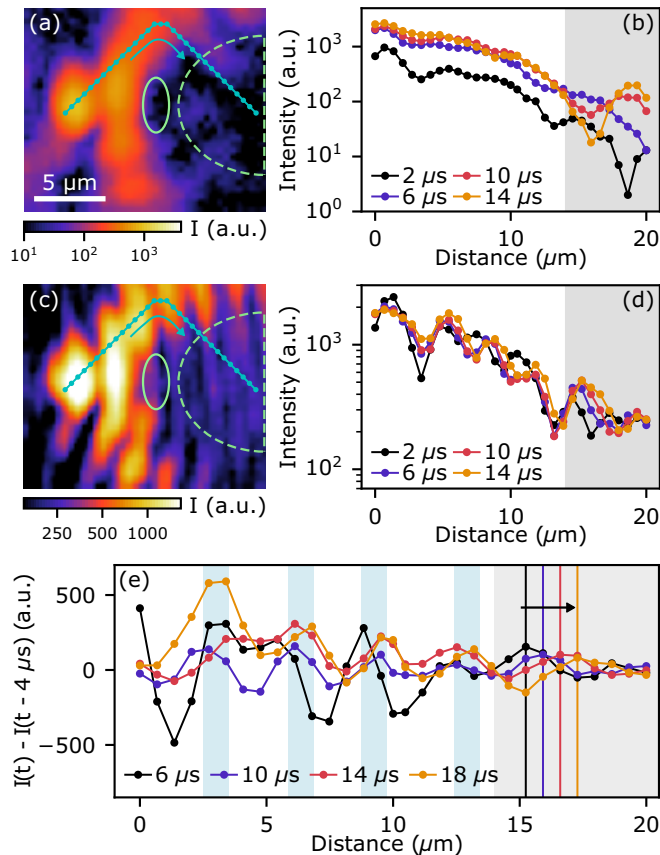


FIG. 8. (a) Position-dependent cavity transmission, as in the top-left panel of Fig. 7. (b) Cut along the path indicated by the blue line in panel (a) for four different times after the step-like power increase. (c) Interferogram due to interfering the cavity transmission with a uniform-phase reference beam, as in the middle-left panel of Fig. 7. (d) Cut along the path indicated by the blue line in panel (c) for four different times after the step-like power increase. (e) Difference in intensity between interferograms recorded 4  $\mu$ s apart in time, evaluated along the path indicated in panel (c). Green ellipses in panels (a) and (c) indicate the position of the obstacle. Shaded regions in panels (b), (d), and (e) indicate the region behind the obstacle. Notice how the peaks in panel (e) align within the blue-shaded rectangles in front of the obstacle, but not behind. Behind the obstacle, the main peak shifts spatially over time as indicated by the vertical lines of the same color as the data plots; this demonstrates an intensity-induced change in the local phase of the photon fluid.

wake of the obstacle. Nonlocality of interactions in space and time have remarkably different consequences. The non-instantaneous nature of the interactions does not alter the properties of the nonscattering steady state; only the duration of the transient scattering regime changes. Spatial nonlocality, in contrast, can surprisingly reduce backscattering when a sufficiently intense fluid of light encounters an obstacle.

For polaritons, the suppression of scattering from a defect was sufficient for the first claim of superfluidity in 2009 [11]. Then, in 2017, the first claim of room-temperature polariton superfluidity was made based on two observations: (i) partial suppression of scattering from an obstacle, and (ii) the emergence of a vortex-antivortex pair in the wake of that obstacle [20]. Further progress in cavity polariton experiments

at cryogenic temperatures enabled the first measurements of the excitation spectrum in 2019 [16], and then in 2022 [19]. Those measurements evinced a linearized excitation spectrum at small momenta, as expected for superfluidity. Our results with photon fluids go beyond what was demonstrated in the first claims of polariton superfluidity by demonstrating a full suppression of scattering and the existence of a critical velocity. However, our results do not include the smoking-gun evidence of superfluidity in the excitation spectrum, which is missing. We hope that our results will nonetheless stimulate further studies of our system, and motivate measurements of the excitation spectrum where a definitive evidence for superfluidity can be sought. Such measurements are not without significant challenges though, given the nonlocal nature of interactions in our system.

The slow rise of the nonlinearity of our system, evinced in Fig. 5, opens up interesting possibilities for experimentally probing the breakdown of Galilean invariance in fluids of light. Indeed, for coherently driven polaritons it has been predicted that an obstacle moving through a stationary fluid is not equivalent to a fluid flowing onto a static obstacle [46]. This breakdown of Galilean invariance arises because the coherently driven polariton field is coupled to a slowly varying exciton reservoir. Consequently, the state of the system is no longer fully determined by the relative velocity between the obstacle and the polariton fluid. The motion of the fluid relative to the reservoir also matters. In polariton systems, the exciton reservoir has a lifetime of a few hundred picoseconds [16]. To observe the breakdown of Galilean invariance in such systems, one would therefore need to move the obstacle across several microns within a few hundred picoseconds or less. Moving an obstacle at such speeds is not impossible, but it is extremely difficult to achieve in practice. In contrast, for our system, probing the breakdown of Galilean invariance seems technologically simpler due to the much slower dynamics of the thermal nonlinearity compared with the exciton reservoir. In our system, the breakdown of Galilean invariance could be probed within a timescale of roughly ten microseconds.

Further perspectives of our results include studies of photon hydrodynamics in complex potential landscapes, and of the interplay of memory and noise [54]. The potential landscape can be tailored using the same technique we used to make the obstacle, or via focused-ion-beam milling [55]. To study the interplay of memory and noise, i.e., non-Markovian dynamics, noise can be added to the laser using modulators [54].

Datasets generated during the current study are stored in a replication package within the AMOLF server. The replication package is available from the corresponding author upon reasonable request. In addition, data for all figures in this paper will be uploaded to the Zenodo repository before publication. Codes for data analysis and numerical calculations are part of the replication package mentioned above and will be uploaded to the Zenodo repository before publication [56].

## ACKNOWLEDGMENTS

This work is part of the research program of the Netherlands Organization for Scientific Research (NWO). We thank

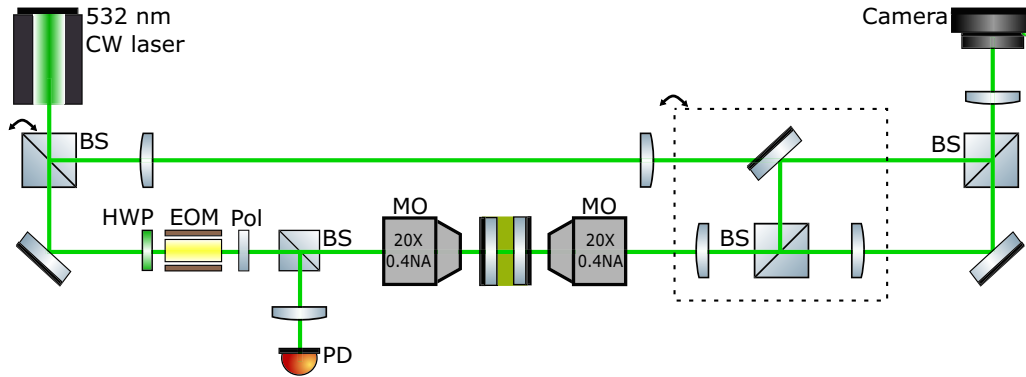


FIG. 9. Schematic of the experimental setup. MO = microscope objective, NA= numerical aperture, CW = continuous wave, EOM = electro-optic modulator, HWP = half wave plate, Pol = linear polarizer, PD = photodetector, BS = beam splitter. This setup was used to make all our measurements.

Ilan Shlesinger, Peter Kirton, and Alberto Amo for stimulating discussions, and Natalia Berloff, Pavlos Lagoudakis, and Pavlos Savvidis for organizing the 2019 HPM conference which stimulated our Collaboration and led to the present results. S.R.K.R. acknowledges an ERC Starting Grant with Project No. 852694.

G.K. performed the experiments, with critical contributions from S.R.K.R., T.H., Z.G., and K.J.H.P. M.W. performed the simulations. S.R.K.R. conceived the experiments and supervised the work. S.R.K.R. and G.K. wrote the paper with critical contributions from M.W. All authors discussed the results and the paper.

The authors declare no competing interests.

#### APPENDIX A: EXPERIMENTAL SETUP

Figure 9 illustrates the experimental setup used for all our measurements. We note that the optical components inside the dashed rectangle in Fig. 9 were removed for the measurements reported in Figs. 5(a)–5(d), 7, and 8; those components were simply unnecessary for those measurements.

#### APPENDIX B: REPRODUCIBILITY OF THE FIG. 8 RESULTS

Figure 8 shows how light flows around the obstacle, and the phase evolves behind but not in front of the obstacle, as scattering is suppressed. Here we present additional data evincing the reproducibility of these effects. We consider the same path indicated by the blue line in Fig. 8(a), and the same four times after the step-like power increase: 2, 6, 10, and 14  $\mu$ s. Results for two different realizations of the same experiment are shown in Fig. 10.

Figures 10(a) and 10(d) show the intensity of the photon fluid, and Figs. 10(b) and 10(e) show the interferogram signal, both along the aforementioned path and at the same times. In correspondence to Fig. 8(e), we also present in Figs. 10(c) and 10(f) an analysis of the intensity difference between interferograms 4  $\mu$ s apart. Overall, these measurements further support the claims in Sec. III by demonstrating the reproducibility of the effects on which those claims are based. In particular, Fig. 10 demonstrates that the light intensity behind the obstacle substantially grows as scattering is suppressed,

and the phase in that region evolves in time. Once again, the latter effect contrasts with the behavior of the phase in front of the obstacle, which is locked to a constant value.

The reproducibility of our results also demonstrates that the onset of the suppression of scattering does not involve permanent deformations in the silicon layer or the adjacent DBR of the mirror containing the obstacle. Such deformations, due to the thermo-optical nonlinearity of silicon, would cause an irreversible change to the potential landscape for photons. Thus, the suppression of scattering is unrelated to the thermo-optical nonlinearity of the silicon layer.

Finally, Fig. 10 shows indications of nonlinearities present in the oil beyond those currently included in the model. Immediately after the step-like power increase, the intensity behind the obstacle increases over time as scattering is suppressed. However, after  $\approx 10$   $\mu$ s, the intensity slightly decreases. The cause for this decrease in intensity is currently unclear to us, and it is not captured by our model. This suggests that there may be additional slow higher-order nonlinearities in our system, which warrant further study. Thus, while our model does not reproduce this feature and its predictions are not in quantitative agreement with our experiments, the simulations qualitatively reproduce the phenomenology presented in Sec. III. This suggests that the dominant mechanisms have been accounted for in our model.

#### APPENDIX C: CALCULATION OF SCATTERING RATIO

Here we describe the method used to calculate the backward and forward scattering at the obstacle,  $I_B$  and  $I_F$ , respectively, based on momentum-space measurements. Since the incident light flows into the positive  $x$  direction, one could conceive ascribing all the intensity in the  $k_x < 0$  region to  $I_B$  and all the intensity in the  $k_x > 0$  region to  $I_F$ . However, in our case that would be inappropriate. We injected light with a broad momentum distribution, and for small average momentum the tail of the distribution significantly extended into the  $k_x < 0$  region. Consequently, ascribing that incident intensity with  $k_x < 0$  to backscattering would be a mistake. To avoid this pitfall, we calculated  $I_B$  and  $I_F$  by fitting Gaussian distributions to parts of the momentum-space measurements as explained next.

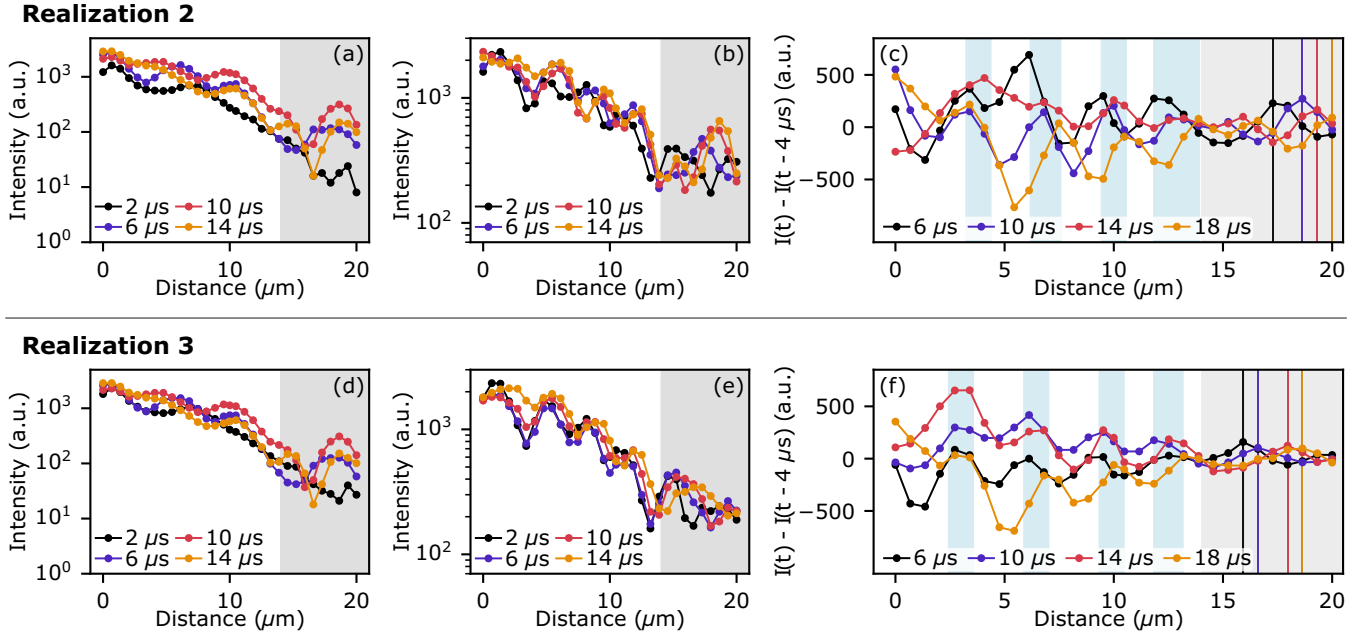


FIG. 10. (a), (d) Spatially dependent transmitted intensity along the trajectory indicated by the blue line in Fig. 8(a). (b), (e) Intensity of interferogram along the trajectory indicated by the blue line in Fig. 8(c). (c), (f) Difference in intensity between interferograms recorded 4  $\mu\text{s}$  apart in time, evaluated along the same trajectory as in panels (b) and (e). Panels (a)–(c) and (d)–(f) correspond to different realizations of the experiment, each distinct from the measurement in Fig. 8. Colored symbols and lines indicate different times after an abrupt increase in input power. Gray-shaded area corresponds to the wake of the obstacle. Fringe maxima before the obstacle align to within the blue rectangles in panels (c) and (f).

Starting from momentum-space measurements such as those shown in Fig. 11(a), we vertically integrated the intensity within  $-0.1 \mu\text{m}^{-1} < k_y < 0.1 \mu\text{m}^{-1}$ . We selected this relatively narrow  $k_y$  range to focus on the forward and backward contributions to the scattering. Our approach avoids smearing out peaks at very different momenta. Moreover, by virtue of the integration, we minimized spurious effects of detector noise.

We started by fitting the integrated intensity with the sum of two Gaussian distributions,

$$f_2(k_x) = A_B \exp\left(\frac{-(k_x - k_B)^2}{2\sigma_B^2}\right) + A_F \exp\left(\frac{-(k_x - k_F)^2}{2\sigma_F^2}\right).$$

$A_{B,F}$ ,  $k_{B,F}$ , and  $\sigma_{B,F}^2$  are the fitted amplitude, mean momentum, and momentum variance of the distributions, respectively. The Gaussians with  $k_F > 0$  and  $k_B < 0$  correspond to the forward- and backward-scattering peaks, respectively. The scattering ratio is then given by  $I_B/I_F = A_B\sigma_B/A_F\sigma_F$ , which is the ratio of the areas under the two Gaussians. The error bars in all our plots of  $I_B/I_F$  correspond to 95% confidence intervals of the fitted values.

In some cases, the fitting function  $f_2(k_x)$  failed to accurately capture the measured lineshape. In those cases, we fitted the lineshape with the sum of three Gaussians:

$$f_3(k_x) = f_2(k_x) + A_3 \exp\left(\frac{-(k_x - k_3)^2}{2\sigma_3^2}\right).$$

$A_3$ ,  $k_3$ , and  $\sigma_3^2$  are the fitted amplitude, mean momentum, and momentum variance of the third Gaussian. If the fit yielded

$k_3 > 0$ , the intensity under the third peak was added to  $I_F$ . Otherwise, it was added to the backscattering. We determined whether the fitting function  $f_3$  (instead of just  $f_2$ ) was at all necessary by calculating the mean squared residuals of the  $f_2$  fit. Only if the mean squared residuals exceed a certain threshold, the data were fitted with  $f_3$ .

Figure 11 illustrates our method for calculating  $I_B/I_F$  in a case where  $f_3$  was needed. Figure 11(a) shows the same data as in Fig. 2(g), with the integration range for  $k_y$  indicated by the green horizontal lines. The integrated intensity within this range is shown as a purple curve in Fig. 11(b). A fit of  $f_3(k_x)$  to the integrated intensity is shown as a dashed green curve. The three Gaussians contributing to the global fit are shown as solid orange curves. The leftmost Gaussian is attributed to backscattering, while the other two correspond to the incident flow.

## APPENDIX D: THEORETICAL MODEL

### 1. Numerical simulations

We model our oil-filled cavity using coupled equations for the light field and the spatial temperature distribution. The equation of motion for the photon field reads (in units of  $\hbar = 1$ )

$$i \frac{\partial}{\partial t} \psi(\mathbf{x}, t) = \left( \epsilon_0 - \frac{i}{2} \gamma - \frac{\nabla^2}{2m^*} + V_D(\mathbf{x}) + \alpha \Delta T(\mathbf{x}, t) \right) \times \psi(\mathbf{x}, t) + F_L(\mathbf{x}) e^{-i\omega_L t + i\mathbf{k}_L \cdot \mathbf{x}}. \quad (\text{D1})$$

Here,  $\epsilon_0$  is the cavity resonance frequency at room temperature,  $m^*$  is the effective photon mass,  $\gamma$  the cavity linewidth,

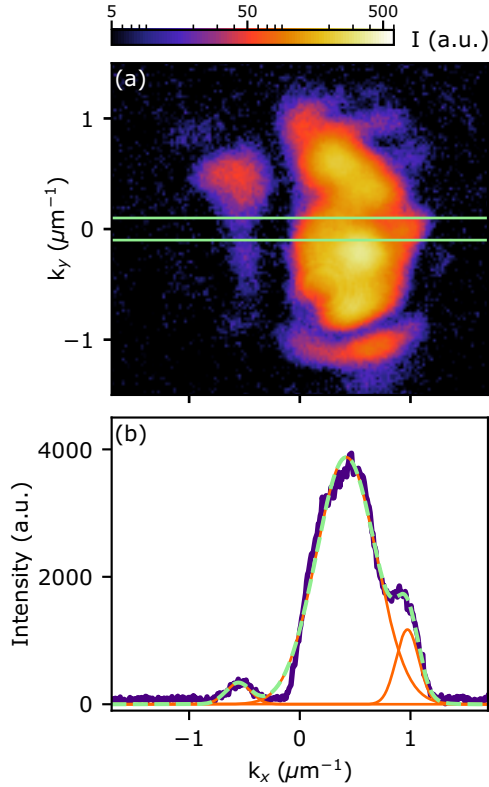


FIG. 11. (a) Transmitted intensity as a function of momentum, same as Fig. 2(g). Horizontal lines indicate the limits for integrating the intensity, as explained in the text. (b) Integrated intensity obtained from panel (a), along with a fit of the function  $f_3$  (sum of three Gaussians) to the data in order to calculate the scattering ratio. Purple curve corresponds to the data, green dashed curve indicates the fit, and orange curves indicate the three Gaussian distributions comprising the fit.

and  $V_D$  is the obstacle potential due to the local deformation of one of the mirrors. The deviation of the temperature from room temperature,  $\Delta T$ , leads to a change in the cavity frequency through the thermo-optic coefficient  $\alpha$ . The coherent laser excitation has amplitude  $F_L$ , frequency  $\omega_L$ , and wave vector  $k_L$ . The temperature dynamics satisfy

$$\frac{\partial}{\partial t} \Delta T(\mathbf{x}, t) = -\gamma_T \Delta T(\mathbf{x}, t) + D_T \nabla^2 \Delta T(\mathbf{x}, t) + \beta |\psi(\mathbf{x}, t)|^2. \quad (\text{D2})$$

$\gamma_T$  is the relaxation rate of the temperature in the transverse direction due to thermal conduction of heat through the mirrors.  $D_T$  is the in-plane thermal diffusion constant.  $\beta$  describes the heating due to photon absorption. The associated pho-

The fluctuations obey the equations of motion

$$i \frac{d}{dt} \begin{pmatrix} u_{\mathbf{k}} \\ v_{\mathbf{k}} \\ w_{\mathbf{k}} \end{pmatrix} = \begin{pmatrix} \frac{(\mathbf{k}_L + \mathbf{k})^2}{2m} - \frac{i}{2} \gamma + \alpha T_0 & 0 & \alpha \sqrt{n_0} \\ 0 & -\frac{(\mathbf{k}_L - \mathbf{k})^2}{2m} - \frac{i}{2} \gamma - \alpha T_0 & -\alpha \sqrt{n_0} \\ i\beta \sqrt{n_0} & i\beta \sqrt{n_0} & -i(\gamma_T + D_T k^2) \end{pmatrix} \begin{pmatrix} u_{\mathbf{k}} \\ v_{\mathbf{k}} \\ w_{\mathbf{k}} \end{pmatrix} + V_0 \sqrt{n_0} \begin{pmatrix} 1 \\ -1 \\ 0 \end{pmatrix}, \quad (\text{D5})$$

where  $V_0$  is the strength of the  $\delta$  potential that acts on the photons, i.e., we take  $V_D = V_0 \delta(x)$ .

ton number decay is included in the photon loss rate  $\gamma$ . A similar model has previously been developed for an incoherently driven thermo-optical photonic cavity [24]. Instead, Eq. (D1) describes a coherently driven system in accordance with the experiment. We numerically solved coupled equations Eqs. (D1) and (D2) using a split step method.

Numerical simulations were performed with  $\gamma = 0.066$  meV,  $k_p = 0.5 \mu\text{m}^{-1}$  and detuning between laser frequency and cavity resonance  $\Delta = \omega_L - \epsilon_0 = 1.2$  meV. The effective photon mass is  $m^* = 0.3 \mu\text{m}^{-2}$  meV $^{-1}$ , which corresponds to  $m^* = 2.1 \times 10^{-35}$  kg. The pump spot is Gaussian shaped with standard deviation  $\sigma_{p_x} = \sigma_{p_y} = 4 \mu\text{m}$ . A Gaussian-shaped obstacle was used, with obstacle potential  $V_0 = 3$  meV and standard deviations  $\sigma_{V_x} = 1 \mu\text{m}$  and  $\sigma_{V_y} = 2 \mu\text{m}$  along and perpendicular to the flow direction, respectively. The obstacle was placed  $10 \mu\text{m}$  from the center of the pump spot. For the simulations shown in Figs. 2(i)–2(p) we used  $D_T = 0.016 \mu\text{m}^2$  meV,  $\gamma_T = 0.001$  meV, and  $\alpha\beta = 0.001$  meV $^2 \mu\text{m}^2$ . Simulations for Figs. 5(e)–5(h) were performed with a  $7 \mu\text{m}$  laser-obstacle distance and  $k_p = 0.2 \mu\text{m}^{-1}$ , and using  $D_T = 0.16 \mu\text{m}^2$  meV,  $\gamma_T = 0.01$  meV, and  $\alpha\beta = 0.01$  meV $^2 \mu\text{m}^2$ . In Fig. 6 the diffusion length was varied by taking  $D_T = 0.001 \mu\text{m}^2$  meV,  $\gamma_T = 0.001$  meV, and  $\alpha\beta = 0.001$  meV $^2 \mu\text{m}^2$  for Figs. 6(a) and 6(c), and  $D_T = 25.6 \mu\text{m}^2$  meV,  $\gamma_T = 0.1$  meV, and  $\alpha\beta = 0.1$  meV $^2 \mu\text{m}^2$  for Figs. 6(b) and 6(d). The total simulation area was  $200 \times 200 \mu\text{m}^2$ .

We note that, based on  $\Delta T$  and the well-known temperature dependence of the oil's refractive index [57], the intensity-dependent refractive index of oil can be quantified [48]. The obtained values are consistent with a nonlinear refractive index  $n_2 = -5 \times 10^{-8}$  cm $^2$ /W, estimated independently via  $z$ -scan measurements [48].

## 2. Bogoliubov theory for uniformly pumped system

When investigating the superfluidity of a resonantly driven photon fluid, the linear-response theory gives valuable information on how a flowing photon fluid responds to the collision with a weak obstacle. We expand the photon field in a homogeneous flow and small fluctuations on top of it:

$$\psi(\mathbf{x}, t) = e^{i\mathbf{k}_L \cdot \mathbf{x} - i\omega_L t} \left[ \sqrt{n_0} + \sum_{\mathbf{k}} (u_{\mathbf{k}}(t) e^{i\mathbf{k} \cdot \mathbf{x}} + v_{\mathbf{k}}^*(t) e^{-i\mathbf{k} \cdot \mathbf{x}}) \right]. \quad (\text{D3})$$

The real temperature field is expanded as

$$T(\mathbf{x}, t) = T_0 + \sum_{\mathbf{k}} (w_{\mathbf{k}} e^{i\mathbf{k} \cdot \mathbf{x}} + w_{\mathbf{k}}^* e^{-i\mathbf{k} \cdot \mathbf{x}}). \quad (\text{D4})$$

The steady state is obtained by setting the time derivative equal to zero. It is instructive to eliminate the temperature

from the steady-state relation through the last row of Eq. (D5), giving

$$w_k = \beta \sqrt{n_0} \frac{u_k + v_k}{\gamma_T + D_T k^2}. \quad (\text{D6})$$

Plugging this expression in the equations for the photonic fluctuations gives

$$\begin{pmatrix} \frac{(k_L+k)^2}{2m} - \frac{i}{2}\gamma + 2gn_0 & gn_0 \\ -gn_0 & -\frac{(k_L-k)^2}{2m} - \frac{i}{2}\gamma - 2gn_0 \end{pmatrix} \begin{pmatrix} u_k \\ v_k \end{pmatrix} + V_0 \sqrt{n_0} \begin{pmatrix} 1 \\ -1 \end{pmatrix} = 0, \quad (\text{D7})$$

with the momentum-dependent interaction strength

$$g(k) = \frac{\alpha\beta}{\gamma_T} \frac{1}{1 + k^2 \ell_T^2}, \quad (\text{D8})$$

where the thermal length is given by

$$\ell_T = \sqrt{D_T/\gamma_T}. \quad (\text{D9})$$

The  $k$  dependence is important only when the momentum is large compared with the inverse of the thermal length or, in other words, when the spatial features are small on the scale of the thermal length. For long spatial scales, much larger than the thermal length, the limit of a zero-range interaction is recovered for what concerns the steady-state response of the system to an obstacle potential.

For our experimental parameters [ $D_T \approx 8 \times 10^{-8}$  m<sup>2</sup>/s and  $\gamma_T = 1/(16 \mu\text{s})$ ], we estimate  $\ell_T \approx 1.13 \mu\text{m}$ , which is rather short on the scale of the observed scattering physics.

Equation (D5) without the external potential determines the excitation spectrum of the system. Since the thermal nonlinearity is slow, it only affects the excitation spectrum very close to  $k = 0$ , for frequencies within a window  $\gamma_T$  around zero.

This brings us in a somewhat peculiar situation where the steady-state scattering off an obstacle is suppressed in complete analogy with a photonic system with instantaneous Kerr nonlinearity, while the excitation spectrum is not distinguishable from the free particle excitation spectrum. The reason for this difference is that the steady-state response to a static obstacle is a zero-frequency property of the system and is therefore not directly related to the dynamical response.

The excitation energies are derived from the real part of the Bogoliubov matrix, where their imaginary part gives information on the stability of the system. For  $k_L = 0$ , instabilities only occur when the photon decay rate and the thermal relaxation rate are of the same order. Since the thermal relaxation time is of the order of  $\mu\text{s}$  and the photon lifetime rather of the order of ps, this poses no problem. For  $k_L \neq 0$  on the other hand, it turns out that instabilities do occur. Some numerical results are presented below.

Figure 12 shows the intensity of scattered photons as a function of the photon density and velocity. The white dotted line indicates the velocity at which the scattering sets in. The intensity of scattered photons can be computed both with the full equations (D5) and with the reduced equations (D7). For what concerns the dynamical stability however, one has to stick to the full set of Eqs. (D5). The red full line gives the

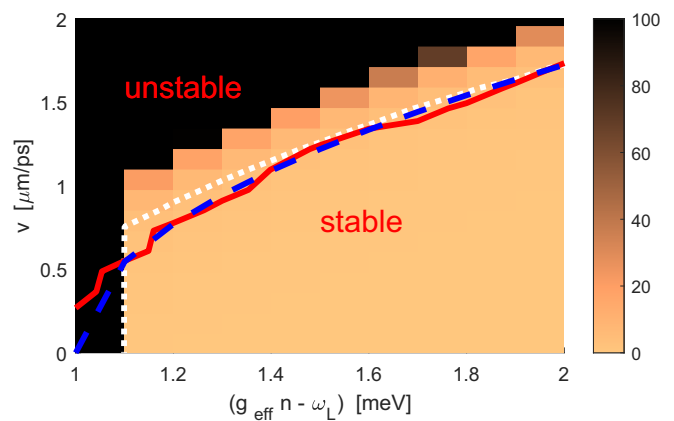


FIG. 12. The intensity of scattered photons (color scale) as a function of the photon density and velocity for  $\omega_L = 1$ ,  $\alpha = 1$ ,  $\beta = \gamma = 6.25 \times 10^{-8}$ , and  $D_T = 8 \times 10^{-8}$ , implying  $\ell_T = 1.13$ . The white dotted line is the contour line at five. The red full line indicates the border of dynamical stability (only stable below). The blue dashed line gives the Landau critical velocity for a system with gapped dispersion.

boundary for dynamical stability (stable for lower velocities below, unstable for higher velocities) and is seen to follow the onset of scattering. This means that the regime of reduced scattering as computed with the effective interaction strength (D8) is dynamically stable. For the regime where scattering takes place however, the reduced model is no longer accurate since it predicts dynamical stability where the full model is actually dynamically unstable. The onset of scattering is well captured by the Landau critical velocity  $v_c = \sqrt{2m\Delta}$  for a system with a gap in the excitation spectrum  $\Delta = g_{\text{eff}}n - \omega_L$ .

## APPENDIX E: CRITICAL VELOCITY MEASUREMENTS

Figure 3 shows the existence of a critical momentum  $k_c$ , and hence a critical velocity, below which backscattering is suppressed. To obtain those results, we followed the fitting approach described above. First we vertically integrated the experimental data in momentum space within the aforementioned  $k_y$  range. Then, we fitted the integrated intensity with either the  $f_2$  or  $f_3$  function. From the fits we extracted the scattering ratio  $I_B/I_F$ , and the mean incident momentum  $k_F$ . The fitted value of  $k_F$  corresponds to the horizontal axis in Fig. 3. The corresponding error bars are 95% confidence intervals on those fits.

## APPENDIX F: MEASUREMENTS EVINCING RECORD SUPPRESSION OF BACKSCATTERING

Figure 4, corresponding to a small flow velocity, evinces a record suppression of backscattering. In this section we present the complete set of measurements from which those results were extracted.

First we show, in Fig. 13(a), the bistability observed in the total transmitted intensity when ramping the incident power up and down. The laser amplitude was modulated sinusoidally at 200 Hz. Next, Figs. 13(b) and 13(c) show the transmitted intensity as a function of position for two incident

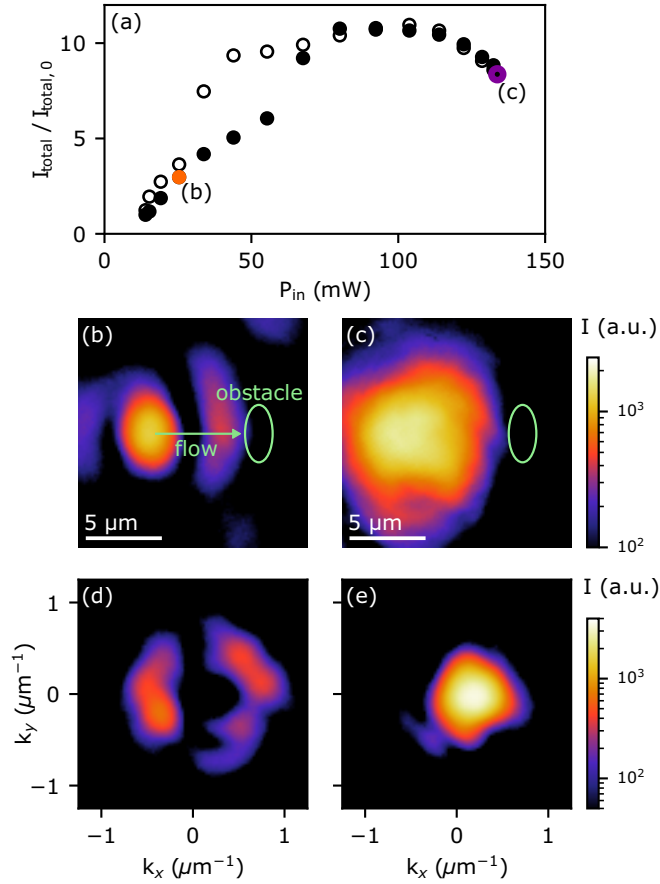


FIG. 13. Record suppression of backscattering above a critical density. Measurements corresponding to the cuts in position and momentum space presented in Figs. 4(a) and 4(b) and scattering ratio calculation in Fig. 4(c). (a) Transmitted intensity when ramping the laser power up and down. (b), (c) Position-space images of transmitted intensity at the laser powers indicated in panel (a). Cuts of panels (b) and (c) along the flow axis are shown in Fig. 4(a) as solid and dashed curves, respectively. Panels (d) and (e) are momentum-space images of the transmitted intensity corresponding to panels (b) and (c), respectively. Cuts of panels (d) and (e) along  $k_y = 0$  are shown in Fig. 4(b) as solid and dashed curves, respectively. Solid and open symbols in panel (a) correspond to increasing and decreasing ramps in power, respectively. Ellipse in panels (b) and (c) indicates the approximate location of the obstacle. Data in panel (a) are normalized to the total intensity at the lowest incident power.

powers. The selected powers are indicated in Fig. 13(a). Figure 13(b), corresponding to a low photon density, shows two fringes resulting from the interference between the incident flow and the scattering off the obstacle. These fringes vanish at high photon density, as Fig. 13(c) shows. Figures 13(d) and 13(e) show momentum-space images corresponding to the measurements in Figs. 13(b) and 13(c). Comparison of Figs. 13(d) and 13(e) reveals the collapse of the Rayleigh scattering ring and the suppression of backscattering at high density. The data in Figs. 4(a) and 4(b) were extracted from the position- and momentum-space images in Figs. 13(b), 13(c) and 13(d), 13(e), respectively. The data in Fig. 4(c) were extracted from momentum-space images, such as those

in Figs. 13(d) and 13(e), following the approach described in Appendix C.

#### APPENDIX G: TEMPERATURE CHANGE IN THE OIL

Here we estimate the temperature rise in the oil at the power needed to observe signatures of photon superfluidity in our system. To that end, we consider how a temperature change in the oil shifts the cavity resonance frequency. The resonance frequency in a planar cavity is given by

$$\omega_0(k) = \omega_0(0) + \frac{\hbar k^2}{2m^*}, \quad (\text{G1})$$

with  $k$  the in-plane wave vector and  $m^*$  the effective photon mass. The resonance frequency at normal incidence is

$$\omega_0(0) = \frac{\pi qc}{nL}, \quad (\text{G2})$$

with  $q$  the longitudinal mode number,  $c$  the speed of light in vacuum,  $n$  the refractive index of the intracavity medium, and  $L$  the cavity length. Using  $m^* = \frac{n^2}{c^2} \hbar \omega_0(0)$  and Eq. (G2), we can write Eq. (G1) as

$$\omega_0(k) = \frac{\pi qc}{nL} + \frac{cL}{2\pi qn} k^2. \quad (\text{G3})$$

Absorption of photons in the oil leads to a change in temperature  $\Delta T$  in the oil, which modifies the refractive index to  $\tilde{n} = n + \delta n$ , where the refractive index change due to the thermo-optical nonlinearity of the oil is given by

$$\delta n = \frac{dn}{dT} \Delta T. \quad (\text{G4})$$

The refractive index change alters the resonance frequency to

$$\tilde{\omega}_0(k) = \left( \frac{\pi qc}{L} + \frac{cL}{2\pi q} k^2 \right) \frac{1}{n + \delta n}. \quad (\text{G5})$$

Based on Ref. [57], we can assume  $\delta n \ll n$  to approximate  $1/(n + \delta n) \approx \frac{1}{n} (1 - \delta n/n)$ . Then, Eq. (G5) reduces to

$$\tilde{\omega}_0(k) \approx \omega_0(k) - \omega_0(k) \frac{\delta n}{n}. \quad (\text{G6})$$

Next, consider the detuning  $\Delta$  between the laser frequency and the cavity resonance frequency,  $\Delta = \omega_L - \omega_0(k)$ . The detuning changes as the resonance frequency shifts upon a temperature change:  $\tilde{\Delta} = \omega_L - \tilde{\omega}_0(k)$ , which using Eq. (G6) we can write

$$\tilde{\Delta} = \Delta + \omega_0(k) \frac{\delta n}{n}. \quad (\text{G7})$$

We now focus on the sonic point, the lowest-intensity point on the upper branch of the bistability, where the excitation spectrum is expected to recover the Bogoliubov dispersion. Importantly, at the sonic point  $\tilde{\Delta} = 0$  [9,10,41]. Using Eqs. (G4) and (G7), this corresponds in our case to

$$\Delta + \omega_0(k) \frac{1}{n} \frac{dn}{dT} \Delta T = 0. \quad (\text{G8})$$

To find the change in temperature at the sonic point, we thus need to solve Eq. (G8) for  $\Delta T$ . We estimate  $\Delta \sim \Gamma$ , with  $\Gamma \approx 0.4$  meV being the cavity linewidth. We use the laser wavelength  $\lambda = 532$  nm to compute  $\omega_L$ . The refractive

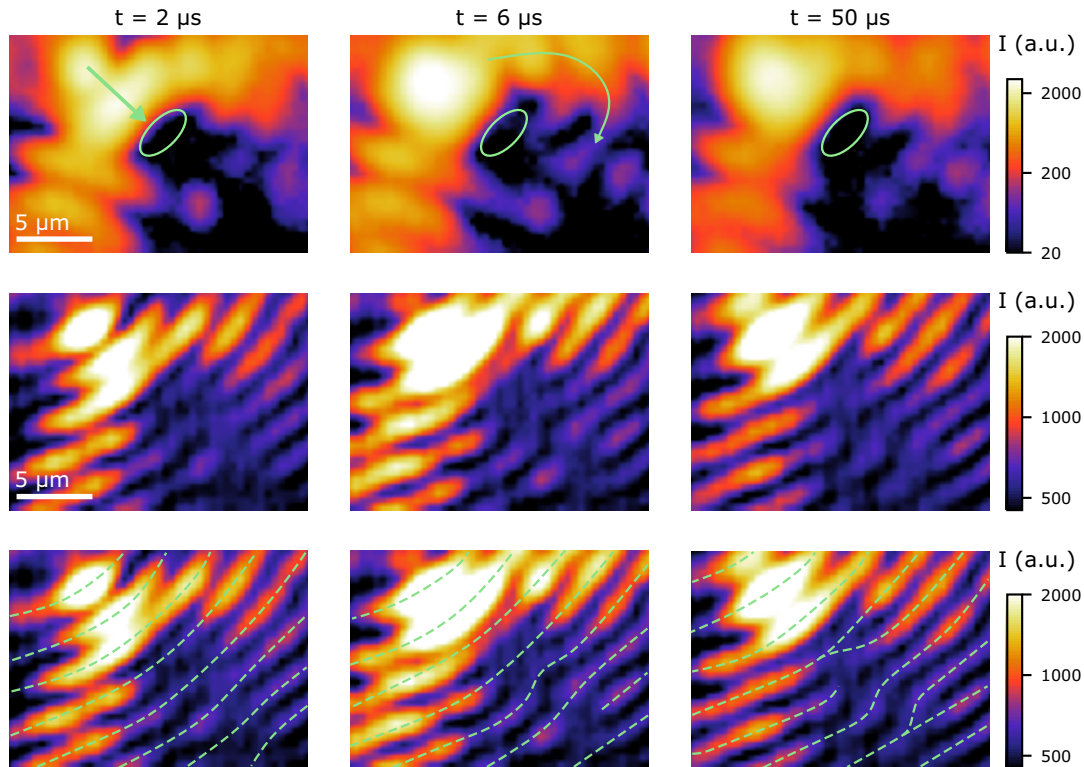


FIG. 14. Free phase evolution in the wake of an obstacle. (top row) Real-space images of transmitted intensity. (middle row) Fringe patterns resulting from the interference between the transmitted intensity and the reference beam. (bottom row) Same as middle row, now with dashed green curves as guides to the eye for fringe maxima. Each column corresponds to a particular time after the rapid increase in input power, as indicated on top. Ellipse indicates approximate location of the obstacle. Arrows indicate the flow direction of the photon fluid.

index of cinnamon oil is  $n \approx 1.59$ , and we estimate  $dn/dT \approx -1 \times 10^{-4}$  based on Ref. [57]. Inserting these parameters, we find the temperature change at the sonic point is  $\Delta T = 2^\circ\text{C}$ . This value is consistent with previous works on oil-filled cavities [48].

#### APPENDIX H: PHASE DISLOCATIONS FOR DIFFERENT FLOW CONDITIONS

Figure 7 shows the emergence of phase dislocations in the wake of an obstacle, where the density of the photon fluid and its mean-field interaction energy decrease. To investigate whether the appearance of phase dislocations is influenced by the specific flow conditions used in Fig. 7, we repeated the experiment for different conditions. Figure 14 shows an example of such measurements. Here, the in-plane angle at which the photon fluid impinges on the obstacle is different from that in Fig. 7.

The top row of Fig. 14 shows the transmitted intensity as a function of position. The middle row shows the interference

of transmitted intensity with a uniform-phase reference beam. These interferometric images are repeated in the bottom row, where dashed green lines have been included as guides to the eye for interference fringe maxima. Each column corresponds to a time elapsed since an abrupt increase in power, as indicated on top.

At  $t = 2 \mu\text{s}$ , the fluid scatters off the obstacle, resulting in fringes upstream of the obstacle in the real-space image. The interferometric measurements show undisturbed phase fronts. At  $t = 6 \mu\text{s}$ , light starts to flow around the obstacle, as indicated by the green arrow. The fringes in the interferometric measurements shift, but no clear dislocations are observed behind the obstacle. When the system has reached the steady state, at  $t = 50 \mu\text{s}$ , the interference fringe from backscattering in the transmitted intensity has disappeared. In the interferometric measurement, phase dislocations have emerged in the immediate wake of the obstacle. Overall, these measurements confirm that the optical phase is not locked in the wake of the obstacle, and that the phase evolves with the intensity for distinct flow conditions.

[1] R. Y. Chiao and J. Boyce, Bogoliubov dispersion relation and the possibility of superfluidity for weakly interacting photons in a two-dimensional photon fluid, *Phys. Rev. A* **60**, 4114 (1999).

[2] E. L. Bolda, R. Y. Chiao, and W. H. Zurek, Dissipative optical flow in a nonlinear Fabry-Pérot cavity, *Phys. Rev. Lett.* **86**, 416 (2001).



- [3] P. Kapitza, Viscosity of liquid helium below the  $\lambda$ -point, *Nature (London)* **141**, 74 (1938).
- [4] J. F. Allen and A. Misener, Flow of liquid helium II, *Nature (London)* **141**, 75 (1938).
- [5] C. Raman, M. Köhl, R. Onofrio, D. S. Durfee, C. E. Kuklewicz, Z. Hadzibabic, and W. Ketterle, Evidence for a critical velocity in a Bose-Einstein condensed gas, *Phys. Rev. Lett.* **83**, 2502 (1999).
- [6] R. Onofrio, C. Raman, J. M. Vogels, J. R. Abo-Shaeer, A. P. Chikkatur, and W. Ketterle, Observation of superfluid flow in a Bose-Einstein condensed gas, *Phys. Rev. Lett.* **85**, 2228 (2000).
- [7] R. Desbuquois, L. Chomaz, T. Yefsah, J. Léonard, J. Beugnon, C. Weitenberg, and J. Dalibard, Superfluid behaviour of a two-dimensional Bose gas, *Nat. Phys.* **8**, 645 (2012).
- [8] L. Pitaevskii and S. Stringari, *Bose-Einstein Condensation and Superfluidity* (Oxford University Press, Oxford, 2016), Vol. 164.
- [9] I. Carusotto and C. Ciuti, Probing microcavity polariton superfluidity through resonant Rayleigh scattering, *Phys. Rev. Lett.* **93**, 166401 (2004).
- [10] I. Carusotto and C. Ciuti, Quantum fluids of light, *Rev. Mod. Phys.* **85**, 299 (2013).
- [11] A. Amo, J. Lefrère, S. Pigeon, C. Adrados, C. Ciuti, I. Carusotto, R. Houdré, E. Giacobino, and A. Bramati, Superfluidity of polaritons in semiconductor microcavities, *Nat. Phys.* **5**, 805 (2009).
- [12] K. G. Lagoudakis, M. Wouters, M. Richard, A. Baas, I. Carusotto, R. André, L. S. Dang, and B. Deveaud-Plédran, Quantized vortices in an exciton-polariton condensate, *Nat. Phys.* **4**, 706 (2008).
- [13] D. Sanvitto, F. Marchetti, M. Szymańska, G. Tosi, M. Baudisch, F. P. Laussy, D. Krizhanovskii, M. Skolnick, L. Marrucci, A. Lemaître *et al.*, Persistent currents and quantized vortices in a polariton superfluid, *Nat. Phys.* **6**, 527 (2010).
- [14] G. Nardin, G. Grosso, Y. Léger, B. Piętko, F. Morier-Genoud, and B. Deveaud-Plédran, Hydrodynamic nucleation of quantized vortex pairs in a polariton quantum fluid, *Nat. Phys.* **7**, 635 (2011).
- [15] A. Amo, S. Pigeon, D. Sanvitto, V. Sala, R. Hivet, I. Carusotto, F. Pisanello, G. Leménager, R. Houdré, E. Giacobino *et al.*, Polariton superfluids reveal quantum hydrodynamic solitons, *Science* **332**, 1167 (2011).
- [16] P. Stepanov, I. Amelio, J.-G. Rousset, J. Bloch, A. Lemaître, A. Amo, A. Minguzzi, I. Carusotto, and M. Richard, Dispersion relation of the collective excitations in a resonantly driven polariton fluid, *Nat. Commun.* **10**, 3869 (2019).
- [17] D. Ballarini, D. Caputo, G. Dagvadorj, R. Juggins, M. De Giorgi, L. Dominici, K. West, L. N. Pfeiffer, G. Gigli, M. H. Szymańska *et al.*, Directional Goldstone waves in polariton condensates close to equilibrium, *Nat. Commun.* **11**, 217 (2020).
- [18] A. Maître, G. Lerario, A. Medeiros, F. Claude, Q. Glorieux, E. Giacobino, S. Pigeon, and A. Bramati, Dark-soliton molecules in an exciton-polariton superfluid, *Phys. Rev. X* **10**, 041028 (2020).
- [19] F. Claude, M. J. Jacquet, R. Usciatì, I. Carusotto, E. Giacobino, A. Bramati, and Q. Glorieux, High-resolution coherent probe spectroscopy of a polariton quantum fluid, *Phys. Rev. Lett.* **129**, 103601 (2022).
- [20] G. Lerario, A. Fieramosca, F. Barachati, D. Ballarini, K. S. Daskalakis, L. Dominici, M. De Giorgi, S. A. Maier, G. Gigli, S. Kéna-Cohen *et al.*, Room-temperature superfluidity in a polariton condensate, *Nat. Phys.* **13**, 837 (2017).
- [21] K. Peng, R. Tao, L. Haeberlé, Q. Li, D. Jin, G. R. Fleming, S. Kéna-Cohen, X. Zhang, and W. Bao, Room-temperature polariton quantum fluids in halide perovskites, *Nat. Commun.* **13**, 7388 (2022).
- [22] R. T. Juggins, J. Keeling, and M. H. Szymańska, Coherently driven microcavity-polaritons and the question of superfluidity, *Nat. Commun.* **9**, 4062 (2018).
- [23] D. Sanvitto, S. Pigeon, A. Amo, D. Ballarini, M. De Giorgi, I. Carusotto, R. Hivet, F. Pisanello, V. G. Sala, P. S. S. Guimaraes, R. Houdré, E. Giacobino, C. Ciuti, A. Bramati, and G. Gigli, All-optical control of the quantum flow of a polariton condensate, *Nat. Photon.* **5**, 610 (2011).
- [24] E. Stein, F. Vewinger, and A. Pelster, Collective modes of a photon Bose-Einstein condensate with thermo-optic interaction, *New J. Phys.* **21**, 103044 (2019).
- [25] E. Stein and A. Pelster, Photon BEC with thermo-optic interaction at dimensional crossover, *New J. Phys.* **24**, 023032 (2022).
- [26] E. Stein and A. Pelster, Hartree-Fock analogue theory of thermo-optic interaction, *New J. Phys.* **25**, 033025 (2023).
- [27] H. Alaeian, M. Schedensack, C. Bartels, D. Peterseim, and M. Weitz, Thermo-optical interactions in a dye-microcavity photon Bose-Einstein condensate, *New J. Phys.* **19**, 115009 (2017).
- [28] W. Wan, S. Jia, and J. W. Fleischer, Dispersive superfluid-like shock waves in nonlinear optics, *Nat. Phys.* **3**, 46 (2007).
- [29] I. Carusotto, Superfluid light in bulk nonlinear media, *Proc. R. Soc. London, Ser. A* **470**, 20140320 (2014).
- [30] D. Vocke, T. Roger, F. Marino, E. M. Wright, I. Carusotto, M. Clerici, and D. Faccio, Experimental characterization of nonlocal photon fluids, *Optica* **2**, 484 (2015).
- [31] D. Vocke, K. Wilson, F. Marino, I. Carusotto, E. M. Wright, T. Roger, B. P. Anderson, P. Öhberg, and D. Faccio, Role of geometry in the superfluid flow of nonlocal photon fluids, *Phys. Rev. A* **94**, 013849 (2016).
- [32] C. Michel, O. Boughdad, M. Albert, P.-É. Larré, and M. Bellec, Superfluid motion and drag-force cancellation in a fluid of light, *Nat. Commun.* **9**, 2108 (2018).
- [33] Q. Fontaine, T. Bienaimé, S. Pigeon, E. Giacobino, A. Bramati, and Q. Glorieux, Observation of the Bogoliubov dispersion in a fluid of light, *Phys. Rev. Lett.* **121**, 183604 (2018).
- [34] D. Vocke, C. Maitland, A. Prain, K. E. Wilson, F. Biancalana, E. M. Wright, F. Marino, and D. Faccio, Rotating black hole geometries in a two-dimensional photon superfluid, *Optica* **5**, 1099 (2018).
- [35] T. D. Ferreira, N. A. Silva, and A. Guerreiro, Superfluidity of light in nematic liquid crystals, *Phys. Rev. A* **98**, 023825 (2018).
- [36] Q. Fontaine, P.-E. Larré, G. Lerario, T. Bienaimé, S. Pigeon, D. Faccio, I. Carusotto, E. Giacobino, A. Bramati, and Q. Glorieux, Interferences between Bogoliubov excitations in superfluids of light, *Phys. Rev. Res.* **2**, 043297 (2020).
- [37] G. Situ and J. W. Fleischer, Dynamics of the Berezinskii-Kosterlitz-Thouless transition in a photon fluid, *Nat. Photon.* **14**, 517 (2020).
- [38] C. Piekarski, W. Liu, J. Steinhauer, E. Giacobino, A. Bramati, and Q. Glorieux, Measurement of the static structure factor in a paraxial fluid of light using Bragg-like spectroscopy, *Phys. Rev. Lett.* **127**, 023401 (2021).
- [39] M. C. Braidotti, R. Prizia, C. Maitland, F. Marino, A. Prain, I. Starshynov, N. Westerberg, E. M. Wright, and D. Faccio,

- Measurement of Penrose superradiance in a photon superfluid, *Phys. Rev. Lett.* **128**, 013901 (2022).
- [40] C. Kurtscheid, D. Dung, A. Redmann, E. Busley, J. Klaers, F. Vewinger, J. Schmitt, and M. Weitz, Realizing arbitrary trapping potentials for light via direct laser writing of mirror surface profiles, *Europhys. Lett.* **130**, 54001 (2020).
- [41] C. Ciuti and I. Carusotto, Quantum fluid effects and parametric instabilities in microcavities, *Phys. Status Solidi B* **242**, 2224 (2005).
- [42] L. Landau, Theory of the superfluidity of helium II, *Phys. Rev.* **60**, 356 (1941).
- [43] T. Frisch, Y. Pomeau, and S. Rica, Transition to dissipation in a model of superflow, *Phys. Rev. Lett.* **69**, 1644 (1992).
- [44] J. Huynh, F. Hébert, M. Albert, and P.-E. Larré, Critical velocity of a two-dimensional superflow past a potential barrier of arbitrary penetrability, *Phys. Rev. A* **109**, 013317 (2024).
- [45] G. Lerario, A. Maître, R. Boddeda, Q. Glorieux, E. Giacobino, S. Pigeon, and A. Bramati, Vortex-stream generation and enhanced propagation in a polariton superfluid, *Phys. Rev. Res.* **2**, 023049 (2020).
- [46] I. Amelio, A. Minguzzi, M. Richard, and I. Carusotto, Galilean boosts and superfluidity of resonantly driven polariton fluids in the presence of an incoherent reservoir, *Phys. Rev. Res.* **2**, 023158 (2020).
- [47] I. Amelio and I. Carusotto, Perspectives in superfluidity in resonantly driven polariton fluids, *Phys. Rev. B* **101**, 064505 (2020).
- [48] Z. Geng, K. J. H. Peters, A. A. P. Trichet, K. Malmir, R. Kolkowski, J. M. Smith, and S. R. K. Rodriguez, Universal scaling in the dynamic hysteresis, and non-Markovian dynamics, of a tunable optical cavity, *Phys. Rev. Lett.* **124**, 153603 (2020).
- [49] A. J. Leggett, *Quantum Liquids: Bose Condensation and Cooper Pairing in Condensed-Matter Systems* (Oxford University Press, Oxford, 2006).
- [50] G. Grosso, G. Nardin, F. Morier-Genoud, Y. Léger, and B. Deveaud-Plédran, Soliton instabilities and vortex street formation in a polariton quantum fluid, *Phys. Rev. Lett.* **107**, 245301 (2011).
- [51] S. Pigeon, I. Carusotto, and C. Ciuti, Hydrodynamic nucleation of vortices and solitons in a resonantly excited polariton superfluid, *Phys. Rev. B* **83**, 144513 (2011).
- [52] S. Pigeon and A. Bramati, Sustained propagation and control of topological excitations in polariton superfluid, *New J. Phys.* **19**, 095004 (2017).
- [53] G. Lerario, S. V. Koniakhin, A. Maître, D. Solnyshkov, A. Zilio, Q. Glorieux, G. Malpuech, E. Giacobino, S. Pigeon, and A. Bramati, Parallel dark-soliton pair in a bistable two-dimensional exciton-polariton superfluid, *Phys. Rev. Res.* **2**, 042041(R) (2020).
- [54] K. J. H. Peters, Z. Geng, K. Malmir, J. M. Smith, and S. R. K. Rodriguez, Extremely broadband stochastic resonance of light and enhanced energy harvesting enabled by memory effects in the nonlinear response, *Phys. Rev. Lett.* **126**, 213901 (2021).
- [55] A. A. P. Trichet, P. R. Dolan, D. M. Coles, G. M. Hughes, and J. M. Smith, Topographic control of open-access microcavities at the nanometer scale, *Opt. Express* **23**, 17205 (2015).
- [56] G. Keijsers, T. Ham, Z. Geng, K. J. H. Peters, M. Wouters, and S. R. K. Rodriguez, Dataset for article “Photon superfluidity through dissipation”, Zenodo, 2024, doi:10.5281/zenodo.11278215.
- [57] S. A. Khodier, Refractive index of standard oils as a function of wavelength and temperature, *Opt. Laser Technol.* **34**, 125 (2002).